

## ABSTRACT

Title of dissertation:      Measuring topology of BECs  
in a synthetic dimensions lattice

Dina Genkina  
Doctor of Philosophy, 2018

Dissertation directed by:   Professor Ian Spielman  
Department of Physics

Measuring topology of BECs in a synthetic dimensions lattice

by

Dina Genkina

Dissertation submitted to the Faculty of the Graduate School of the  
University of Maryland, College Park in partial fulfillment  
of the requirements for the degree of  
Doctor of Philosophy  
2018

Advisory Committee:  
Professor Ian Spielman, Chair/Advisor

© Copyright by  
Dina Genkina  
2018



# Table of Contents

List of Tables	6
List of Figures	7
2 Atom Light Interactions	1
2.1 Near-resonant atom-light interaction . . . . .	1
2.2 Absorption imaging . . . . .	2
2.3 One dimensional optical lattices . . . . .	5
2.3.1 Far off-resonant atom-light interaction . . . . .	5
2.3.2 Lattice Hamiltonian . . . . .	7
2.3.3 Tight binding approximation . . . . .	11
2.3.4 Pulsing vs adiabatic loading of the lattice . . . . .	12
2.4 Raman and rf coupling . . . . .	17
2.4.1 Hyperfine structure . . . . .	17
2.4.2 Rf coupling Hamiltonian . . . . .	19
2.4.3 Raman coupling Hamiltonian . . . . .	21
2.4.4 Calibration of Raman and Rf dressed states . . . . .	24
6 Synthetic Magnetic Fields in Synthetic Dimensions	30
6.1 Synthetic dimensions setup . . . . .	31
6.2 Hamiltonian of the effective 2-D system . . . . .	34
6.2.1 Hamiltonian . . . . .	34
6.2.2 Band structure . . . . .	36
6.2.3 Calibration . . . . .	39
6.2.4 Tight binding approximation . . . . .	42
6.3 Eigenstates of the synthetic 2-D lattice . . . . .	44
6.4 Chiral edge currents . . . . .	46
6.5 Observation of skipping orbits . . . . .	49
Bibliography	52

## List of Tables

## List of Figures

1	Absorption imaging. (a) Near resonant probe light illuminates the atoms, and the transmitted light (containing a shadow of the atoms) is imaged on the camera. A second image taken with no atoms provides a reference. (b) The probe beam is partially absorbed as it traverses the cloud, and the intensity seen by atoms further along the imaging direction $e_z$ is lowered. (c) An atomic cloud illuminated by a probe light field absorbs photons from the probe and re-emits them in all directions. This process results in a net acceleration of the cloud in the direction of the probe light as well as diffusive spreading in the transverse directions. . . . .	3
2	Lattice band structure in the extended zone scheme. The dashed lines represent the limit of zero lattice depth, with the regular parabolic dispersion relation of a free particle repeating with reciprocal lattice period. The solid lines are the dispersion relation at $V_0 = 4.0E_L$ , showing the opening of gaps at crossings of the zero lattice depth bands. The black lines demarcate the first Brillouin zone. . . . .	10
3	Lattice pulsing. (a) Lattice depth as a function of time during a pulsing experiment. The lattice is turned on instantaneously at $t = 0$ and held on for a variable amount of time until being turned off instantaneously at a final time $t = t_f$ . (b) Atomic population before $t = 0$ . The dispersion relation is that of a free particle, and all of the atoms start out at $q = 0$ in the lowest energy level. Here, the area of the dots is proportional to the fractional population in the energy state. (c) Atomic population after the lattice is turned on for a lattice depth of $V_0 = 8.0E_L$ . The energy spectrum now shows the lattice band structure, and some atomic population is projected onto the excited bands. (d) Atomic population after the lattice is snapped off at $t_f = 150 \mu s$ . The wavefunction is projected back onto the bare states, with some fraction (blue circle) in the lowest band at $k = 0$ and some fraction in the excited band, with equal population being projected onto the $k = 2k_L$ (green) and $k = -2k_L$ (red). . . . .	14

4	Lattice pulsing for calibration. (a) An example time-of-flight image from a pulsing experiment. The three different clouds are different momentum orders. (b) Fractional populations in the different momentum orders as a function of pulsing time at a low lattice power. Data is indicated by dots and best fit theory is represented by lines. The lattice depth from fit is $V_0 = 5.57 \pm 0.07 E_L$ . (c) Fractional populations in the different momentum orders as a function of pulsing time at a higher lattice power. Data is indicated by dots and best fit theory is represented by lines. The lattice depth from fit is $V_0 = 12.69 \pm 0.07 E_L$ .	15
5	Adiabatic lattice loading. (a) Lattice depth as a function of time during adiabatic turn-on. The lattice is ramped on starting at $t = 0$ , slowly increasing to a final lattice depth and turned off instantaneously at a final time $t = t_f$ . (b) Atomic population before $t = 0$ . All atoms are at $k = 0$ in the lowest bare band. (c) Atomic population after the lattice is turned on adiabatically to a lattice depth of $V_0 = 8.0 E_L$ . All atoms remain in the lowest band, but the band is no longer bare. (d) Atomic population after the lattice is snapped off. The wavefunction is projected back onto the bare states, with some fraction (blue circle) in the lowest band at $k = 0$ and some fraction in the excited band, with equal population being projected onto the $k = 2k_L$ (green) and $k = -2k_L$ (red). Since the lowest lattice band is a superposition of bare bands, some atoms are excited to the higher bare bands.	16
6	Energy structure of hyperfine states of the ground state of $^{87}\text{Rb}$ as a function of external magnetic field strength in Gauss. Figure from ref. [1]	18
7	Raman and rf coupling schematic. (a) Beam geometry of the Raman beams and rf relative to the external field. The Raman beams have a frequency difference $\Delta\omega$ , and are linearly polarized in perpendicular directions. (b) Level structure of both Raman and Rf coupling for hyperfine states of the $F = 1$ manifold. The hyperfine splitting separates the levels by an energy $\hbar\omega_z$ . The quadratic Zeeman shift $\epsilon$ lowers the energy of the $m_F = 0$ state, and the detuning $\delta$ of either the Raman or the rf fields shifts the energies of the $m_F = \pm 1$ states. Raman transitions are two-photon, exciting up to a virtual state and coming back down to an adjacent hyperfine state, with an accompanying momentum transfer. Rf couples adjacent hyperfine states directly. Figure taken from ref. [2]	20
8	Band structure of the rf Hamiltonian, Eq. 2.28, in momentum space. For all plots, the quadratic Zeeman shift $\hbar\epsilon = 0.04 E_R$ , and the color represents magnetization, labeled by the colorbar. (a) $\hbar\Omega = 0$ , $\hbar\delta = 0$ . No coupling or detuning is present, so the only separation between the bands is due to the quadratic shift $\hbar\epsilon$ . (b) $\hbar\Omega = 5.0 E_R$ , $\hbar\delta = 0$ . (c) $\hbar\Omega = 0$ , $\hbar\delta = 1.0 E_R$ . Even though the coupling strength is zero, the bands are separated by the detuning. (d) $\hbar\Omega = 5.0 E_R$ , $\hbar\delta = 1.0 E_R$ .	22



9	Band structure of the Raman Hamiltonian, Eq. 2.31, in momentum space. For all plots, the quadratic Zeeman shift $\hbar\epsilon = 0.04E_R$ , and the color represents magnetization, labeled by the colorbar. (a) $\hbar\Omega = 0$ , $\hbar\delta = 0$ . (b) $\hbar\Omega = 1.0E_R$ , $\hbar\delta = 0$ . (c) $\hbar\Omega = 5.0E_R$ , $\hbar\delta = 0.0$ . (d) $\hbar\Omega = 0.0$ , $\hbar\delta = 1.0E_R$ . (e) $\hbar\Omega = 1.0E_R$ , $\hbar\delta = 1.0E_R$ . (f) $\hbar\Omega = 5.0E_R$ , $\hbar\delta = 1.0E_R$ . . . . .	25
10	Pulsing on rf coupling. (a) Example time-of-flight image during an rf pulsing experiment in the $F = 1$ manifold. Spin states are separated via a Stern-Gerlach pulse along the horizontal direction. (b) Example time-of-flight image during an rf pulsing experiment in the $F = 2$ manifold. Here, 5 spin components are present. (c) Pulsing experiment in the $F = 1$ manifold. Dots represent fractional populations in different spin states measured from time-of-flight images, and lines represent best fit theory curves. Fitted parameters are $\hbar\Omega = 0.863 \pm 0.004E_R$ , $\hbar\delta = -0.198 \pm 0.007E_R$ . (d) Pulsing experiment in the $F = 2$ manifold. Dots represent fractional populations in different spin states measured from time-of-flight images, and lines represent best fit theory curves. Fitted parameters are $\hbar\Omega = 1.000 \pm 0.002E_R$ , $\hbar\delta = -0.061 \pm 0.001E_R$ . $\hbar\epsilon = 0.038E_R$ for all panels. . . . .	27
11	Pulsing on Raman coupling. (a) Example time-of-flight image during a Raman pulsing experiment in the $F = 1$ manifold. A Stern-Gerlach pulse during time-of-flight separates different spin components along the horizontal direction, and different momentum orders fly apart along the vertical direction. (b) Fractional population in different spin states during a Raman pulsing experiment as a function of time. Dots represent data and lines represent a best fit from theory. The fitted parameters are $\hbar\Omega = 1.47 \pm 0.01E_R$ , $\hbar\delta = 0.004 \pm 0.024E_R$ . The quadratic Zeeman shift was $\hbar\epsilon = 0.038E_R$ . . . . .	28
1	Setup of effective 2-D lattice. (a) Beam geometry. The BEC is subject to a bias magnetic field $B_0$ in the $\mathbf{e}_z$ direction. The 1-D lattice beam and Raman beams are both along the $\mathbf{e}_x$ direction, and the rf field can be applied with projections onto both the $\mathbf{e}_x$ and $\mathbf{e}_y$ . (b) Schematic of the effective 2-D lattice. Sites along $\mathbf{e}_x$ are formed by the 1-D optical lattice and labelled by site number $j$ . Sites along the synthetic direction $\mathbf{e}_s$ are formed by the spin states: 3 sites for atoms in the $F = 1$ manifold and 5 sites for atoms in $F = 2$ . These sites are labelled by $m$ . Raman transitions induce a phase shift, which can be gauge transformed into a tunneling phase along the $\mathbf{e}_x$ direction. This leads to a net phase when hopping around a single lattice plaquette of $\phi_{AB}$ . . . . .	32

2	Band structure of the synthetic dimensions Hamiltonian, eqn. 6.4. For all panels, the detuning $\hbar\delta = 0$ and the quadratic shift $\hbar\epsilon = 0.02E_L$ . (a) $F = 1$ , $\hbar\Omega = 0.0$ . (b) $F = 1$ , $\hbar\Omega = 0.5$ . (c) $F = 2$ , $\hbar\Omega = 0.0$ . (d) $F = 2$ , $\hbar\Omega = 0.5$ . . . . .	37
3	Calibration of synthetic dimesnions lattice. (a) Ramping procedure. The blue line represents the 1-D lattice depth as a function of time and the red line represents Raman coupling as a function of time. Both are held on for a variable amount of time $t$ , producing Rabi oscillations. (b) Example of fractional populations in different $m$ states as a function of time $t$ in the $F = 1$ manifold. Dots indicate data and lines indicate the best fit to theory, with parameters $\hbar\Omega = 0.56 \pm 0.01E_L$ and $\hbar\delta = 0.029 \pm 0.002E_L$ . (c) Example time-of-flight image in the $F = 1$ manifold. A Stern-Gerlach gradient pulse separates different $m$ states along the horizontal axis, while the lattice and Raman beams give momentum along the vertical axis. (d) Example of fractional populations in different $m$ states as a function of time $t$ in the $F = 2$ manifold. Dots indicate data and lines indicate the best fit to theory, with parameters $\hbar\Omega = 0.61 \pm 0.002E_L$ and $\hbar\delta = 0.002 \pm 0.001E_L$ . (e) Example time-of-flight image in the $F = 2$ manifold. A Stern-Gerlach gradient pulse separates different $m$ states along the horizontal axis, while the lattice and Raman beams give momentum along the vertical axis. . . . .	40
4	Band structure of the tight binding versus full Hamiltonian. $V_0 = 6.0E_L$ , giving $t_x = 0.1E_L$ , $\hbar\delta = 0$ , $\hbar\epsilon = 0.02E_L$ , $\hbar\Omega = 0.5E_L$ . (a) $F = 1$ , fitted value $t_s = 0.154E_L$ . (b) $F = 2$ , fitted value $t_s = 0.284$ . . . . .	43
5	Eigenstates of the synthetic dimensions lattice. Left column: time-of-flight images, with position along $\mathbf{e}_s$ on the vertical axis and momentum along $\mathbf{e}_s$ on the horizontal. Right column: fractional populations in each site $m$ . (a,b) Rf coupling, resulting in $\phi_{AB} = 0$ . (c,f) Raman coupling, resulting in $\phi_{AB} > 0$ , adiabatically loaded from the $m_F = 1$ state. (d,g) Raman coupling, resulting in $\phi_{AB} > 0$ , adiabatically loaded from the $m_F = 0$ state. (c,f) Raman coupling, resulting in $\phi_{AB} > 0$ , adiabatically loaded from the $m_F = -1$ state. . . . .	45

- 6 Measuring chiral currents in synthetic dimensions. (a) Schematic of the formation of chiral currents when the system is loaded into the bulk  $m = 0$  site and tunneling along  $\mathbf{e}_s$  is turned on suddenly. (b) Fractional population in each spin state as a function of time for a system with  $\phi_{AB} > 0$ . Dots represent data and lines represent theory, with parameters  $\hbar\Omega = 0.5E_L$ ,  $V_0 = 6E_L$ ,  $\hbar\delta = 0.001E_L$ , and  $\hbar\epsilon = 0.05E_L$ . (c) Chiral current  $\mathcal{I}$  as a function of time for  $\phi_{AB} > 0$  (red)  $\phi_{AB} = 0$  (empty black dots) and  $\phi_{AB} < 0$  (solid black). (d) Chiral current  $\mathcal{I}$  as a function of  $\langle|m|\rangle$  for the three values of  $\phi_{AB}$ . Solid lines calculated from theory, with the same parameters as in (b) for  $\phi_{AB} \neq 0$ , and with parameters  $\hbar\Omega = 0.33E_L$ ,  $V_0 = 6E_L$ ,  $\hbar\delta = -0.01E_L$ , and  $\hbar\epsilon = 0.05E_L$  for  $\phi_{AB} = 0$ . (e) Peak chiral current  $\mathcal{I}_{\max}$  as a function of tunneling asymmetry  $t_s/t_x$ . Inset: slope of best fit lines of current  $\mathcal{I}$  as a function of  $\langle|m|\rangle$  (as in (d)) as a function of tunneling asymmetry  $t_s/t_x$ : nearly independent. . . . . 48
- 7 Imaging skipping orbits. (a) Schematic of pulsing experiment when atoms are initialized on the edge. (b) Schematic of the tilted box potential applied along the synthetic direction. (c) Expectation value of position along  $\mathbf{e}_s$ ,  $\langle m \rangle$ , as a function of pulse time for atoms initialized in the  $m = +1$  (red) and  $m = -1$  (blue) states. Dots represent data and lines are from theory with parameters  $\hbar\Omega = 0.41E_L$ ,  $V_0 = 5.2E_L$ ,  $\hbar\delta = \pm 0.087E_L$ , and  $\hbar\epsilon = 0.13E_L$ . (d) Expectation value of the group velocity along  $\mathbf{e}_x$ ,  $\langle v_x \rangle$ , for the same data as in (c). (e) Expectation value of displacement along  $\mathbf{e}_x$ ,  $\langle \delta j \rangle$  in units of lattice spacing, for the same data as in (c) and (d). The displacement was obtained by integrating  $\langle v_x/a \rangle$ , where  $a$  is the period of the optical lattice. Atoms initialized in  $m = -1$  performed skipping orbits to the left, while atoms starting in  $m = +1$  travelled to the right. . . . . 50

## Chapter 2: Atom Light Interactions

### 2.1 Near-resonant atom-light interaction

In this section, we will assume the atom can be treated as a two-level system: one with a ground and excited atomic state, with an energy difference of energy difference  $\hbar\omega_0$ . When such an atom, starting in the ground state, is illuminated by a laser beam with frequency  $\hbar\omega_L$ , there are three kinds of transitions that occur: during absorption the atom absorbs a photon from the laser and goes from the ground to the excited state; during stimulated emission, the atom emits a photon into the field of the laser beam and jumps from the excited to the ground state; during spontaneous emission, the atom decays to the ground state from the excited state with no help from the laser, emitting into a random vacuum mode. Stimulated emission results in coherent light co-propagating with the laser beam, while spontaneous emission results in light scattering incoherently in any direction. The rate of spontaneous emission from an excited state is given by the natural transition linewidth of the transition  $\Gamma$ .

On timescales short compared to  $1/\Gamma$ , spontaneous emission can be ignored, and an atom undergoes coherent Rabi oscillations between the ground and excited states via cycles of absorption and stimulated emission [3]. Taking  $c_g$  and  $c_e$  to be the time-dependent coefficients multiplying the eigenstate wavefunctions of the ground and excited state respectively, and assuming the atom starts in the ground

state  $c_g(t = 0) = 1$ , the excited state population is given by

$$c_e(t) = -i \frac{\Omega}{\Omega'} \sin\left(\frac{\Omega' t}{2}\right) e^{-i\delta t/2}, \quad (2.1)$$

where  $\Omega$  is the Rabi frequency given by  $\Omega^2 = \frac{\Gamma \lambda_L^3}{h(2\pi)^3} I$ , with  $\lambda_L$  as the laser wavelength,  $h$  as Plank's constant and  $I$  as the laser intensity,  $\Omega' = \sqrt{\Omega^2 + \delta^2}$  is the generalized Rabi frequency and  $\delta = \omega_0 - \omega_L$  is the detuning of the laser from atomic resonance.

In the regime where spontaneous emission cannot be ignored, Rabi oscillations of each individual atom are intermittently interrupted by decay to the ground state. Averaging over an atomic ensemble, on the time scale of a single Rabi oscillation the overall excited state population reaches a steady state, and the rate of spontaneous emission becomes constant. Since during spontaneous emission the ejected photon can go into any vacuum mode, this process can be thought of as the scattering of photons by the atoms. This scattering rate is given by [3]

$$\gamma_{\text{sc}} = \frac{\Gamma}{2} \frac{I/I_{\text{sat}}}{1 + 4(\delta/\Gamma)^2 + I/I_{\text{sat}}}, \quad (2.2)$$

where  $I_{\text{sat}}$  is the saturation intensity. This is the intensity at which the timescale of spontaneous emission matches the Rabi oscillation rate, reducing the capacity for absorption of extra light.

## 2.2 Absorption imaging

Absorption imaging takes advantage of the on-resonant interaction described in the previous section. An on or near-resonant laser beam ( $\delta/\Gamma \ll 1$ ) is shined at the atoms, and the absorbed light acts to create a shadow in the shape of the atoms in the laser beam. This beam with the shadow is then imaged on a camera, in our case a CCD, as depicted in Figure 1a (top). This is called the atom image,

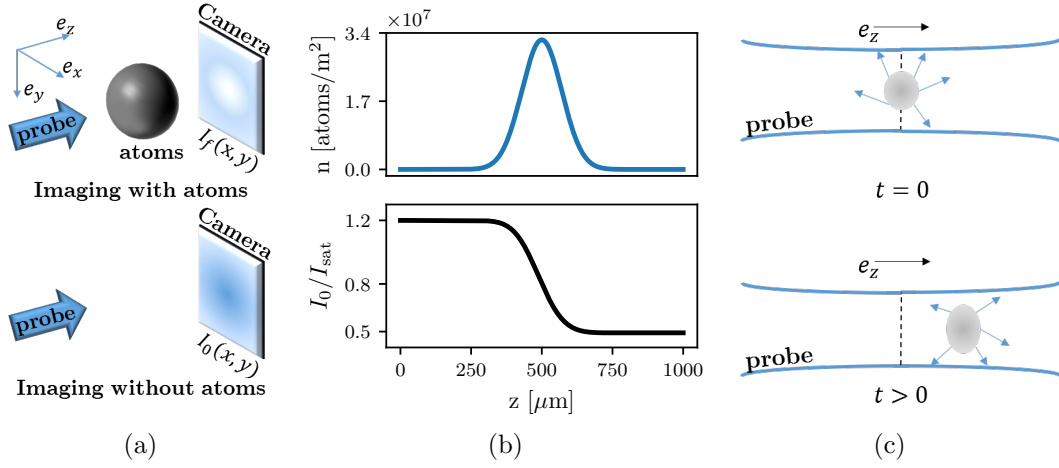


Figure 1: Absorption imaging. (a) Near resonant probe light illuminates the atoms, and the transmitted light (containing a shadow of the atoms) is imaged on the camera. A second image taken with no atoms provides a reference. (b) The probe beam is partially absorbed as it traverses the cloud, and the intensity seen by atoms further along the imaging direction  $e_z$  is lowered. (c) An atomic cloud illuminated by a probe light field absorbs photons from the probe and re-emits them in all directions. This process results in a net acceleration of the cloud in the direction of the probe light as well as diffusive spreading in the transverse directions.

and the intensity distribution over the camera is denoted by  $I_f(x, y)$ , where the subscript f stands for final - the intensity after the light has encountered the atoms. To quantify the 'shadowed out' intensity, after the atoms have left the trap the same laser intensity is shined directly at the camera, as in Figure 1a (bottom). This is called the probe image, and the intensity distribution over the camera is denoted by  $I_0(x, y)$ , where the subscript 0 indicated initial - the intensity before the light had encountered the atoms.

To recover the atom number distribution encountered by the light, consider an atomic cloud with 3D density  $\rho(x, y, z)$ . Since we can only obtain 2D information from the camera, we can only hope to recover a 2D atomic column density  $n(x, y) = \int \rho(x, y, z) dz$ . Focusing in on a single pixel of the camera, we can consider a single value of  $I_0$  and  $I_f$  to recover a local  $n$ . As the laser light propagates through the atomic cloud, the intensity of the light will diminish due to absorption. This

absorption as a function of propagation direction  $z$  can be expressed using the scattering rate equation Eq. 2.2 as the number of photons scattered by the atoms (proportional to the atomic density times the scattering rate) times the photon energy  $\hbar\omega_L$ :

$$\frac{d}{dz} \frac{I(z)}{I_{\text{sat}}} = -\hbar\omega_L \rho(z) \gamma_{sc}(z) = -\rho(z) \sigma_0 \frac{I(z)/I_{\text{sat}}}{1 + 4\delta^2/\Gamma^2 + I(z)/I_{\text{sat}}}, \quad (2.3)$$

where the resonant scattering cross section is  $\sigma_0 = 3\lambda_0^2/2\pi$ , and  $\lambda_0$  is the wavelength associated with atomic resonance.

Integrating both sides of Eq. 2.3, we obtain

$$\sigma_0 n = (1 + 4\delta^2/\Gamma^2) \ln(I_0/I_f) + (I_0 - I_f)/I_{\text{sat}}. \quad (2.4)$$

The quantity  $OD = \ln(I_0/I_f)$  is called the optical depth of the cloud. When the probe intensity  $I_0$  is much smaller than the saturation intensity, the second term in Eq. 2.4 becomes negligible. Assuming further that the probe light is on resonance,  $\delta = 0$ , the atomic column density becomes simply  $\sigma_0 n = OD$ . Figure 1b shows a Gaussian atomic density distribution (top) and the resulting probe intensity as a function of position in the cloud (bottom). The intensity drops from its initial to final value gradually as it traverses the cloud.

However, there is an important effect that the above equations do not account for. Namely, as the atoms absorb light from the probe beam, they also get a momentum kick equal to the momentum of a photon during each collision  $\hbar k_r = h/\lambda_L$  in the direction of propagation. It is true that the absorbed photon will then be re-emitted by the atom, inducing a loss of momentum, but since this happens through the process of spontaneous emission into a random vacuum mode, the average momentum kick acquired this way over many re-emissions will average to zero. On average, each photon absorbed will induce a change in velocity of the atom of  $v_r = \hbar k_r/m$ ,

where  $m$  is the atomic mass, as depicted in Fig. 1c. As the velocity of the atom changes, due to the Doppler effect, the apparent laser frequency will change as well. Therefore, even if the laser light is exactly on-resonant for a stationary atom, it will become off-resonant for longer imaging times, and Eq. 2.3 will acquire a time dependence. For most experiments, this effect is small and can be neglected. However, if the imaging time becomes of order a recoil time  $t_r$ , a time after which the recoil-induced detuning  $\delta$  becomes of order  $\Gamma$ , this effect becomes significant. We explore this effect in Chapter ??.

## 2.3 One dimensional optical lattices

### 2.3.1 Far off-resonant atom-light interaction

As described in section 2.1, on timescales where spontaneous emission can be neglected, two-level atoms exposed to laser radiation undergo coherent Rabi oscillations between the two levels. Starting with  $c_g$  and  $c_e$  as the time-dependent coefficients multiplying the eigenstate wavefunctions of the ground and excited state respectively, and assuming the atom starts in the ground state  $c_g(t = 0) = 1$ , we make the traditional transformation to the rotating frame:

$$c'_g(t) = c_g(t) \tag{2.5}$$

$$c'_e(t) = c_e(t)e^{-i\delta t}, \tag{2.6}$$



where  $\delta$  is the detuning of laser light from resonance. In this frame, we can write the atom-light Hamiltonian in the  $\begin{pmatrix} c'_g \\ c'_e \end{pmatrix}$  basis as:

$$H = \hbar \begin{pmatrix} -\delta/2 & \Omega/2 \\ \Omega/2 & \delta/2 \end{pmatrix}, \quad (2.7)$$

where  $\Omega$  is the coupling strength, also known as the Rabi frequency. In the limit of no coupling,  $\Omega = 0$ , in the rotating frame the eigenenergies are  $E_{\pm} = \pm\hbar\delta/2$ . For non-zero coupling, finding the eigenvalues of  $H$  gives  $E_{\pm} = \pm\hbar\sqrt{\delta^2 + \Omega^2}/2$ . Therefore, the bare (without light) eigenenergies are shifted in the presence of the light.

For a far detuned laser beam, one expects that no absorption of the light will actually take place, and the atom will remain entirely in the ground state. Indeed, solving the Shroedinger equation with the above Hamiltonian

$$i\hbar \frac{d}{dt} \begin{pmatrix} c'_g \\ c'_e \end{pmatrix} = H \begin{pmatrix} c'_g \\ c'_e \end{pmatrix} \quad (2.8)$$

we obtain the oscillating excited state population

$$c'_e(t) = -i \frac{\Omega}{\sqrt{\Omega^2 + \delta^2}} \sin \left( \frac{\sqrt{\Omega^2 + \delta^2} t}{2} \right), \quad (2.9)$$

where the amplitude of the oscillation approaches zero in the limit  $\Omega \ll \delta$ . Thus, the only effect of the light in this regime is to shift the eigenenergies of the ground and excited states. Expanding the energies in the small parameter  $\Omega/\delta$ , we obtain the shifted energies  $E_{\pm} = \pm\hbar\sqrt{\delta^2 + \Omega^2}/2 \approx \pm(\delta/2 + \Omega^2/4\delta)$ . The shift from bare energy levels is thus

$$\Delta E_{\pm} = \pm\Omega^2/4\delta. \quad (2.10)$$

This laser intensity dependent energy shift is called the AC Stark shift, and is the basis of most laser created potentials for cold atoms.

For the ground state, and a red detuned laser beam (where the laser frequency is lower than the resonant frequency), this creates energy minima in locations of maximal laser intensity. For the lattice described in this chapter, as well as for the trapping of our atoms in the final stages of cooling, we use high power (up to 10 W) lasers with wavelength  $\lambda_L = 1064$  nm.

### 2.3.2 Lattice Hamiltonian

Our 1-D optical lattice is created by retro-reflecting the  $\lambda_L = 1064$  nm laser, creating a standing wave of light. Via the AC Stark shift, this creates a periodic potential for the atoms of the form

$$V = V_0 \sin^2(k_L x), \quad (2.11)$$

where  $k_L = 2\pi/\lambda_L$  is the wavenumber associated with the lattice recoil momentum. The time-independent Hamiltonian, for some eigenenergy  $E_n$ , will be given by

$$-\frac{\hbar^2}{2m} \frac{d^2}{dx^2} \Psi_n(x) + V_0 \sin^2(k_L x) \Psi_n(x) = E_n \Psi_n(x). \quad (2.12)$$

Since the potential is spatially periodic, we can invoke Bloch's theorem [4]:

$$\Psi_{n,q} = e^{iqx} u_{n,q}(x), \quad (2.13)$$

where  $q$  is the crystal momentum restricted to  $\pm \hbar k_L$ , and  $u_{n,q}(x)$  is the spatially varying part of the wavefunction. Plugging this in to the Hamiltonian, we obtain

$$-\frac{\hbar^2}{2m} \left( -q^2 + 2iq \frac{d}{dx} + \frac{d^2}{dx^2} \right) u_{n,q}(x) + V_0 \sin^2(k_L x) u_{n,q}(x) = E_n u_{n,q}(x). \quad (2.14)$$

Expanding  $u_{n,q}(x)$  in Fourier components commensurate with the lattice period of  $2k_L$  as  $u_{n,q}(x) = \sum_{j=-\inf}^{\inf} a_j e^{i2k_L j x}$ , we obtain

$$\sum_j \left( \frac{\hbar^2}{2m} (q + 2k_L)^2 a_j + V_0 \sin^2(k_L x) a_j \right) e^{i2k_L j x} = E_n \sum_j a_j e^{i2k_L j x}. \quad (2.15)$$

Re-writing  $\sin^2(k_L x) = (e^{-2ik_L x} + e^{2ik_L x} - 2)/4$ , multiplying both sides by  $e^{i2k_L j' x}$  and invoking  $\sum_j c_j e^{ik(j-j')} = \delta_{jj'}$ , where  $\delta_{jj'}$  is the Kroniker delta and  $c_j$  are appropriately normalized coefficients, we get for any value of the index  $j$

$$\frac{\hbar^2}{2m} (q + 2k_L j)^2 a_j - \frac{V_0}{4} (a_{j+1} + a_{j-1}) = E_n a_j. \quad (2.16)$$

This can be expressed in matrix form

$$H_L = \begin{pmatrix} \ddots & & & & & \\ & \frac{\hbar^2}{2m} (q + 4k_L)^2 & \frac{V_0}{4} & 0 & 0 & 0 \\ & \frac{V_0}{4} & \frac{\hbar^2}{2m} (q + 2k_L)^2 & \frac{V_0}{4} & 0 & 0 \\ & 0 & \frac{V_0}{4} & \frac{\hbar^2}{2m} q^2 & \frac{V_0}{4} & 0 \\ & 0 & 0 & \frac{V_0}{4} & \frac{\hbar^2}{2m} (q - 2k_L)^2 & \frac{V_0}{4} \\ & & 0 & 0 & \frac{V_0}{4} & \frac{\hbar^2}{2m} (q - 4k_L)^2 \\ & & & & & \ddots \end{pmatrix}, \quad (2.17)$$

in the basis of momentum orders  $|k\rangle = e^{ikx}$  given by:

$$\begin{pmatrix} \vdots \\ |q + 4k_L\rangle \\ |q + 2k_L\rangle \\ |q\rangle \\ |q - 2k_L\rangle \\ |q - 4k_L\rangle \\ \vdots \end{pmatrix}. \quad (2.18)$$

This matrix can be diagonalized for every value of the crystal momentum  $q$ , with the resulting band structure shown in Figure 2. It is convenient to define the lattice recoil energy  $E_L = \hbar^2 k_L^2 / 2m$ . Then, we can re-write the Hamiltonian with  $V_0$  in units of  $E_L$  and momenta  $q$  in units of  $k_L$  as

$$H_L/E_L = \begin{pmatrix} \ddots & & & & & \\ & (q+4)^2 & \frac{V_0}{4} & 0 & 0 & 0 \\ & \frac{V_0}{4} & (q+2)^2 & \frac{V_0}{4} & 0 & 0 \\ & 0 & \frac{V_0}{4} & q^2 & \frac{V_0}{4} & 0 \\ & 0 & 0 & \frac{V_0}{4} & (q-2)^2 & \frac{V_0}{4} \\ & & 0 & 0 & \frac{V_0}{4} & (q-4)^2 \\ & & & & & \ddots \end{pmatrix}. \quad (2.19)$$

In any numerical simulation, the number of momentum orders that can be included is finite. We determine the value of the parameter  $n = \max(|j|)$  as the lowest  $n$  at which the eigenvalues stop changing to machine precision from  $n - 1$ . The code for finding and plotting the eigenvalues and eigenvectors of the lattice hamiltonian is included in Appendix [MAKE APPENDIX WITH CODE?].

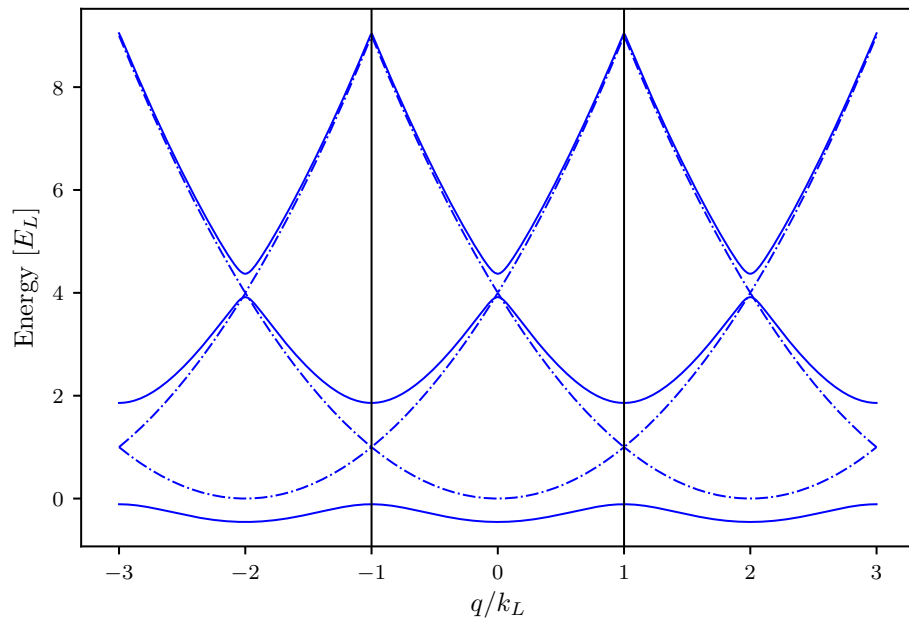


Figure 2: Lattice band structure in the extended zone scheme. The dashed lines represent the limit of zero lattice depth, with the regular parabolic dispersion relation of a free particle repeating with reciprocal lattice period. The solid lines are the dispersion relation at  $V_0 = 4.0E_L$ , showing the opening of gaps at crossings of the zero lattice depth bands. The black lines demarcate the first Brillouin zone.

### 2.3.3 Tight binding approximation

In the limit of large lattice depths,  $V_0 > \approx 5E_L$ , the lattice Hamiltonian is well approximated by the tight-binding model. In the tight binding model, the basis is assumed to be a set of orthogonal functions, called Wannier functions, localized to each lattice site  $|j\rangle$ . The approximation lies in assuming only nearest neighbor tunnelings between the sites, forming the tight-binding Hamiltonian

$$H_{\text{tb}} = -t |j\rangle \langle j+1| + \text{H.c.}, \quad (2.20)$$

where  $t$  is the tunneling amplitude between nearest neighbor sites and H.c. stands for Hermitian conjugate. We have neglected the diagonal kinetic energy term, as it will be equal for every Wannier function  $|j\rangle$  and thus represents a constant energy offset. All the information about the lattice depth is therefore reflected in the tunneling amplitude  $t$ .

The tight binding Hamiltonian can also be expressed in the momentum basis by Fourier transforming the basis functions:

$$|j\rangle = \frac{1}{\sqrt{N}} \sum_{k_j} e^{-ik_j j} |k_j\rangle, \quad (2.21)$$

giving the Hamiltonian

$$H_{\text{tb}} = -\frac{1}{N} \sum_{k_1} \sum_{k_2} k_2 t e^{-ik_1 j} e^{ik_2(j+1)} |k_1\rangle \langle k_2| + \text{H.c} = 2t \cos(k) |k\rangle \langle k|. \quad (2.22)$$

From this we can directly read off the band structure of the tight binding Hamiltonian. First, we notice that we only obtain one band - to approximate higher bands with the tight binding approximation we would need to construct a different set of Wannier functions and a different tunneling strength. Second, we see that the lowest

band is simply a cosine - therefore we have solved for the band structure without even defining what the basis Wannier functions are! Third, the amplitude of the cosine function is given by the tunneling strength  $t$ . This gives us a good clue as to how to determine the appropriate tunneling given a lattice depth  $V_0$  - simply find a  $t$  that matches the amplitude of the lowest band, which becomes cosinusoidal in the deep lattice limit.

The precise form of the Wannier functions depends on both the depth of the lattice and the band being reproduced. It is not necessary for us to find their full expression, as the band structure can be calculated without them. The definition, however, is

$$|j\rangle = \int_{\text{BZ}} e^{i\phi(q)-iqja} \Psi_q(x) dq, \quad (2.23)$$

where the integral is over the Brillouin zone, from  $-k_L$  to  $k_L$ ,  $a$  is the lattice spacing  $\lambda_L/2$ , and  $\Psi_q$  is the Bloch wavefunction at crystal momentum  $q$ , and  $\phi(q)$  is the phase associated with each Bloch wavefunction. The Bloch wavefunctions individually have arbitrary phase. The phase plays an important role in combining the Bloch wavefunctions into a Wannier function, finding the proper phase relationship to make the wavefunction maximally localized at each site [5].

### 2.3.4 Pulsing vs adiabatic loading of the lattice

The lattice depth parameter  $V_0/4$ , for a range of values, can be well calibrated experimentally by pulsing on the lattice. Here, the word pulsing indicates that the lattice is turned on fully non-adiabatically, if not instantaneously, such that the original bare momentum state is projected onto the lattice eigenbasis, as shown in Figure 5a. If the atoms start out stationary in the trap, the bare state in the

momentum basis is simply

$$|\Psi_0\rangle = \begin{pmatrix} \vdots \\ 0 \\ 0 \\ 1 \\ 0 \\ 0 \\ \vdots \end{pmatrix}, \quad (2.24)$$

as depicted in Figure 5b.

Since the lattice eigenbasis is distinct from the bare one, instantaneously turning on the lattice will necessarily excite the atoms into a superposition of lattice eigenstates, each evolving with a different phase according to the eigenenergy while the lattice is on, as shown in Figure 5c. Then, when the lattice is snapped back off, the wavefunction is projected back into the bare basis, and the varying phase accumulation results in a beating of the different momentum orders, see Figure 5d. This can be calculated simply by using the time evolution operator

$$|\Psi(t)\rangle = e^{-iH_L t/\hbar} |\Psi_0\rangle. \quad (2.25)$$

By pulsing on the lattice for variable amounts of time  $t$ , we can obtain fractional populations in the different momentum states. Time-of-flight imaging captures the momentum distribution of the cloud, and the different entries of  $\Psi(t)$  in the momentum basis will thus appear as different clouds on the absorption image, as shown in Figure 4a. The fractional population in these clouds corresponds to a measurement of  $|a_j|^2$ . Typically for our values of the lattice depth  $V_0 < 10E_L$ , it is sufficient to simply count three central momentum orders,  $k = q, q \pm 2k_L$ . Then, we can fit Eq. 2.25 to the data with fitting parameter  $V_0$ , thus deducing the lattice depth. Some



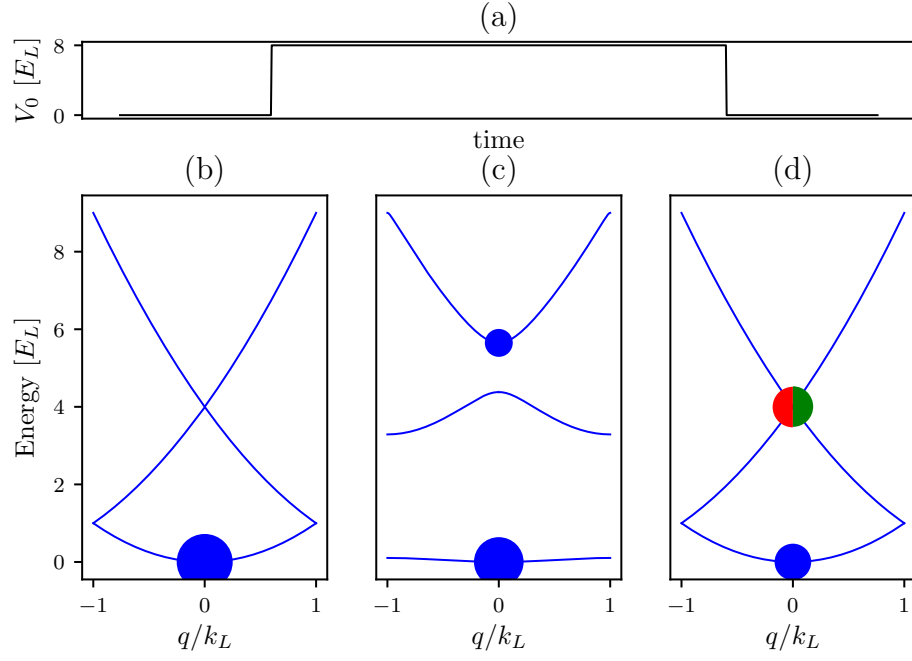


Figure 3: Lattice pulsing. (a) Lattice depth as a function of time during a pulsing experiment. The lattice is turned on instantaneously at  $t = 0$  and held on for a variable amount of time until being turned off instantaneously at a final time  $t = t_f$ . (b) Atomic population before  $t = 0$ . The dispersion relation is that of a free particle, and all of the atoms start out at  $q = 0$  in the lowest energy level. Here, the area of the dots is proportional to the fractional population in the energy state. (c) Atomic population after the lattice is turned on for a lattice depth of  $V_0 = 8.0 E_L$ . The energy spectrum now shows the lattice band structure, and some atomic population is projected onto the excited bands. (d) Atomic population after the lattice is snapped off at  $t_f = 150 \mu s$ . The wavefunction is projected back onto the bare states, with some fraction (blue circle) in the lowest band at  $k = 0$  and some fraction in the excited band, with equal population being projected onto the  $k = 2k_L$  (green) and  $k = -2k_L$  (red).

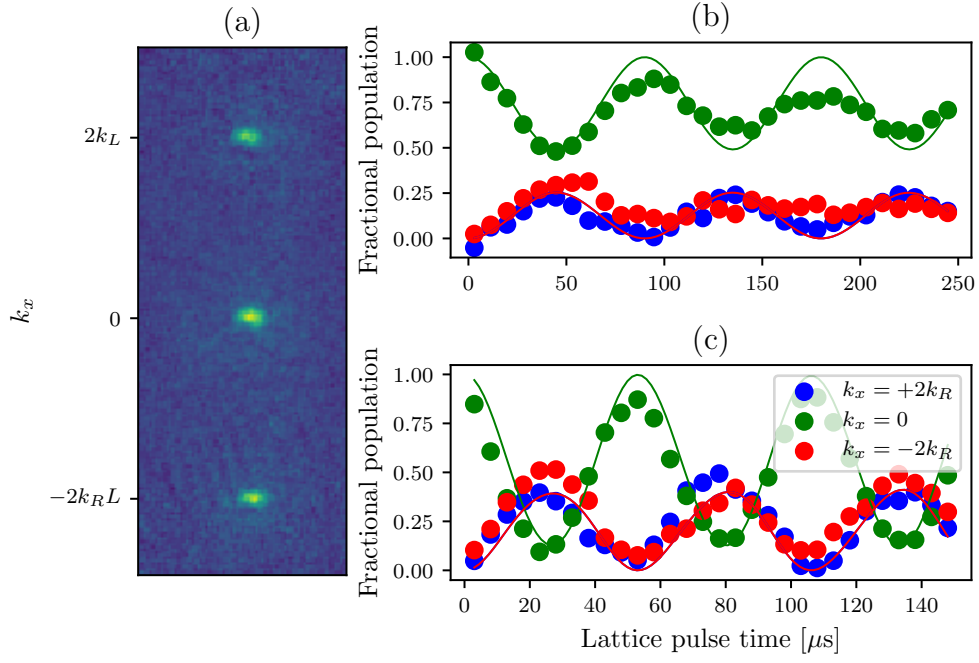


Figure 4: Lattice pulsing for calibration. (a) An example time-of-flight image from a pulsing experiment. The three different clouds are different momentum orders. (b) Fractional populations in the different momentum orders as a function of pulsing time at a low lattice power. Data is indicated by dots and best fit theory is represented by lines. The lattice depth from fit is  $V_0 = 5.57 \pm 0.07 E_L$ . (c) Fractional populations in the different momentum orders as a function of pulsing time at a higher lattice power. Data is indicated by dots and best fit theory is represented by lines. The lattice depth from fit is  $V_0 = 12.69 \pm 0.07 E_L$ .

examples of these pulsing experiments are presented in figure 4b,c.

In contrast to pulsing, adiabatic loading turns the lattice on slowly, such that the atomic wavefunction starting in the bare ground state can continuously adjust to remain in the ground state of the current Hamiltonian, without projecting onto any of the higher bands. This process is illustrated in Figure 5. The adiabatic timescale depends on the spacing between the ground and next excited band (or if starting in a different eigenstate, the nearest eigenstate). If the energy difference between the ground and first excited state is  $\Delta E$ , the timescale on which the lattice is turned on must fulfill  $t \gg \hbar/\Delta E$ .

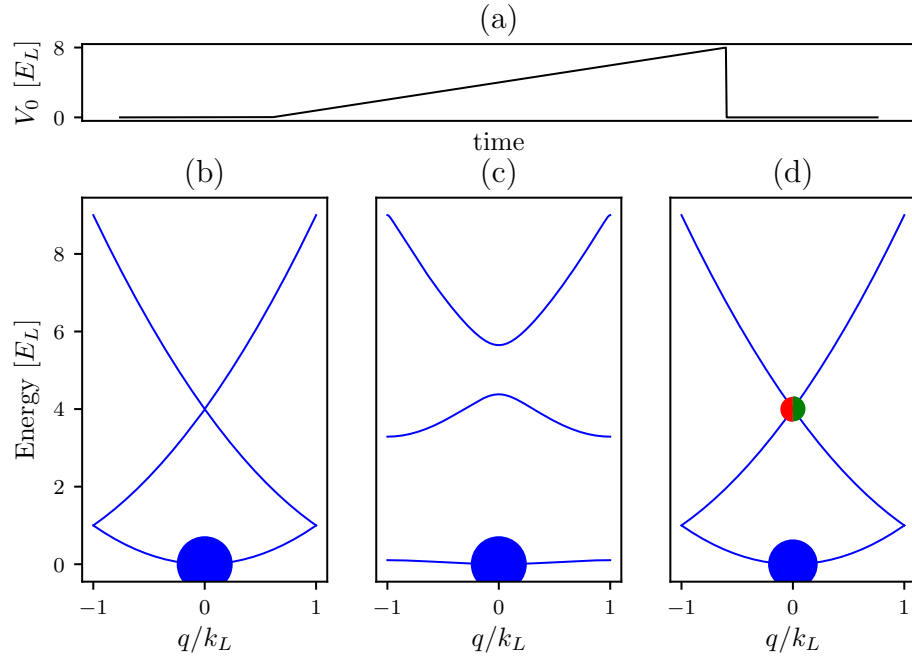


Figure 5: Adiabatic lattice loading. (a) Lattice depth as a function of time during adiabatic turn-on. The lattice is ramped on starting at  $t = 0$ , slowly increasing to a final lattice depth and turned off instantaneously at a final time  $t = t_f$ . (b) Atomic population before  $t = 0$ . All atoms are at  $k = 0$  in the lowest bare band. (c) Atomic population after the lattice is turned on adiabatically to a lattice depth of  $V_0 = 8.0E_L$ . All atoms remain in the lowest band, but the band is no longer bare. (d) Atomic population after the lattice is snapped off. The wavefunction is projected back onto the bare states, with some fraction (blue circle) in the lowest band at  $k = 0$  and some fraction in the excited band, with equal population being projected onto the  $k = 2k_L$  (green) and  $k = -2k_L$  (red). Since the lowest lattice band is a superposition of bare bands, some atoms are excited to the higher bare bands.

## 2.4 Raman and rf coupling

### 2.4.1 Hyperfine structure

Alkali atoms' energy levels can be understood as primarily the energy state of the single electron in the outer shell. Fine structure arises from different combinations of angular momenta, including orbital angular momentum of the outermost electron with respect to the nucleus  $\mathbf{L}$ , the electron spin  $\mathbf{S}$  and the nuclear spin  $\mathbf{I}$ . The total electron angular momentum is the combination of orbital and the spin angular momenta  $\mathbf{J} = \mathbf{L} + \mathbf{S}$ , and the quantum number can be any integer  $|L - S| \leq J \leq |L + S|$ . The ground state of  $^{87}\text{Rb}$ , in term notation  $^{2S+1}L_J$  is  $^2S_{1/2}$ , where  $S$  is orbital notation indicating  $L = 0$ . Since the total spin quantum number  $J = 1/2$ , this produces two possible spin projection quantum numbers,  $m_J = \pm 1/2$ .

There is also a contribution from the nuclear spin  $\mathbf{I}$ , resolvable at low magnetic fields, which gives rise to hyperfine structure of the states. For  $^{87}\text{Rb}$ ,  $I = 3/2$ . The total spin, including nuclear spin, is indicated by the quantum number  $F$ , and  $|J - I| \leq F \leq |J + I|$ . The interaction with the nuclear spin splits the ground state of  $^{87}\text{Rb}$  into two manifolds,  $F = 1$  and  $F = 2$ , with three hyperfine states in the  $F = 1$  manifold ( $m_F = 0, \pm 1$ ) and five hyperfine states in the  $F = 2$  manifold ( $m_F = 0, \pm 1, \pm 2$ ). These states couple to an external magnetic field  $B_z$  along some direction  $\mathbf{e}_z$  via the Hamiltonian  $H_B = \mu_B(g_J J_z + g_I I_z)B_z/\hbar$ . Here  $\mu_B$  is the Bohr magneton, and  $g_J$  and  $g_I$  are Lande g-factors. Since  $g_J \gg g_I$ , at high fields the nuclear spin interaction becomes small compared to the total energy shift, and the levels are grouped according to their  $m_J$  quantum number, as seen in Figure 6.

At low fields, however, the states are approximately linearly dependent on the  $m_F$  quantum number. The linear shift from the  $B = 0$  states is known as the linear Zeeman shift. In the intermediate regime, the correction to the linear shift can be expressed in terms of an energy correction to each hyperfine state  $\epsilon(B)|m_F|^2$ ,

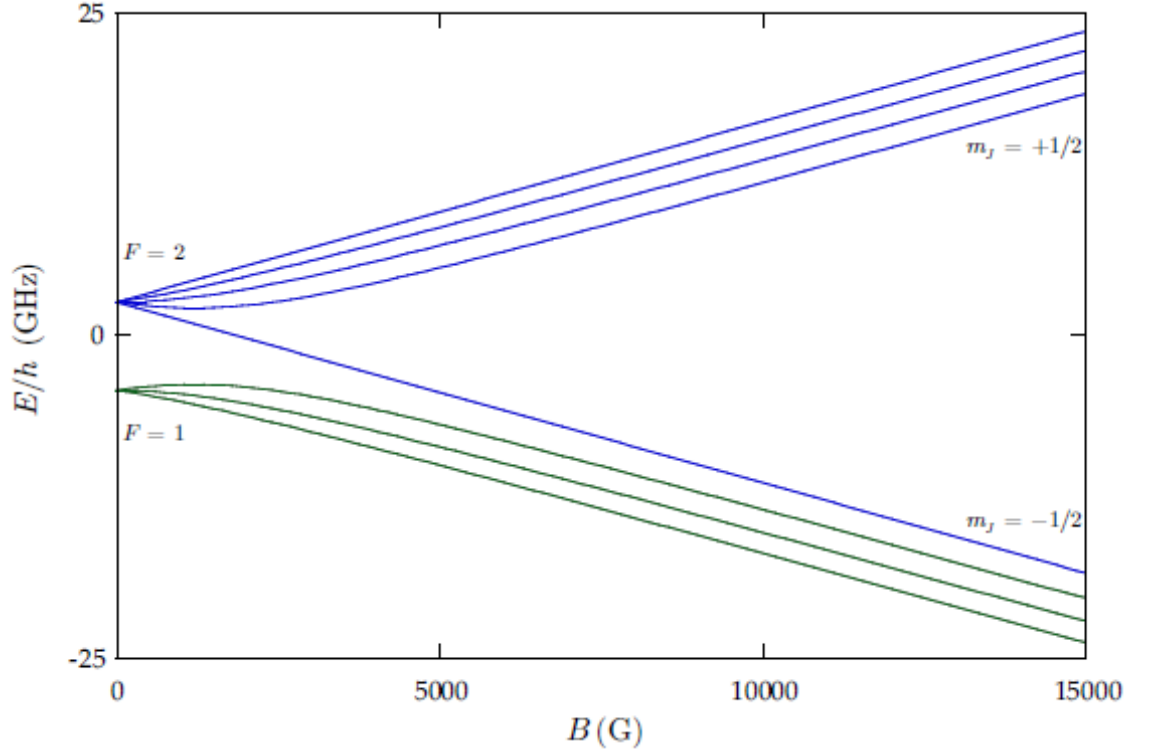


Figure 6: Energy structure of hyperfine states of the ground state of  $^{87}\text{Rb}$  as a function of external magnetic field strength in Gauss. Figure from ref. [1]

known as the quadratic Zeeman shift. For the magnetic fields used in experiments described in this thesis, this correction is sufficient for describing the energy levels.

The form of the Hamiltonian in this regime for any value of  $F$  is given by

$$H_0 = H_{\text{KE}} + \hbar\omega_z \mathbf{F}_z + \hbar\epsilon \mathbf{F}_z^2, \quad (2.26)$$

where  $\hbar\omega_z = \mu_B g_F B_z / \hbar$ , and the kinetic energy Hamiltonian  $H_{\text{KE}} = \hbar^2 \vec{k}^2 / 2m\mathcal{I}$ , and  $\mathcal{I}$  is the identity matrix.

### 2.4.2 Rf coupling Hamiltonian

For the  $F = 1$  manifold, there are three available spin states  $m_F = 0, \pm 1$ . There are many ways of introducing coupling terms between the different hyperfine states. Here, we will explain two methods: rf coupling and Raman coupling. Rf coupling is a radio-frequency oscillating magnetic field, in our case produced by a pair of circular coils in series side by side above the atoms (see [6]). Assuming the rf oscillating field is polarized along the  $\mathbf{e}_x$ , with the bias field along  $\mathbf{e}_z$ , the coupling Hamiltonian is given by  $H_{rf} = \mu_B g_F \vec{\mathbf{F}} \cdot \vec{\mathbf{B}} = \mu_B g_F \mathbf{F}_x B_x \cos(\omega t)$ , where  $2\pi\omega$  is the rf frequency. The schematic of this setup is shown in Figure 7. The eigenstates of the bare Hamiltonian  $H_0$  are the constituent  $m_F$  states. The eigenstates of the coupled Hamiltonian  $H_0 + H_{rf}(t)$  can be expressed as a linear superposition of the bare eigenstates  $\Psi(\vec{x}, t) = \sum_{m_F} c_{m_F}(t) \phi_{m_F}(\vec{x}) e^{-i\omega_{m_F} t}$ . The Hamiltonian in this basis can then be written as [3]

$$H_{\text{rf}} = H_{\text{KE}} + \hbar \begin{pmatrix} 0 & \Omega \cos(\omega t) e^{i\omega_z t} & 0 \\ \Omega \cos(\omega t) e^{-i\omega_z t} & 0 & \Omega \cos(\omega t) e^{i\omega_z t} \\ 0 & \Omega \cos(\omega t) e^{-i\omega_z t} & 0 \end{pmatrix}, \quad (2.27)$$

where  $\Omega$  is the Rabi frequency, proportional to  $B_x$ . We can then transfer into the rotating frame  $c'_{m_F} = e^{-im_F \delta t} c_{m_F}$ , where  $\delta = \omega_z - \omega$ . Then we apply the rotating wave approximation, that the fast oscillating terms average to zero over time scales of interest  $e^{2i\omega t} \approx 0$ , and obtain

$$H_{\text{rf}} = H_{\text{KE}} + \hbar \begin{pmatrix} \delta & \Omega/2 & 0 \\ \Omega/2 & -\epsilon & \Omega/2 \\ 0 & \Omega/2 & -\delta \end{pmatrix}, \quad (2.28)$$

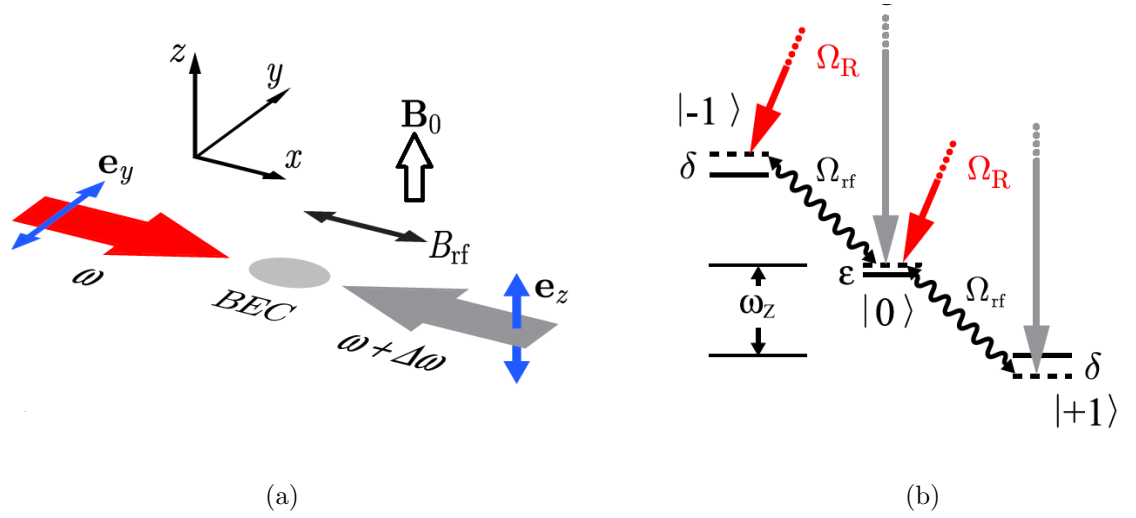


Figure 7: Raman and rf coupling schematic. (a) Beam geometry of the Raman beams and rf relative to the external field. The Raman beams have a frequency difference  $\Delta\omega$ , and are linearly polarized in perpendicular directions. (b) Level structure of both Raman and Rf coupling for hyperfine states of the  $F = 1$  manifold. The hyperfine splitting separates the levels by an energy  $\hbar\omega_z$ . The quadratic Zeeman shift  $\epsilon$  lowers the energy of the  $m_F = 0$  state, and the detuning  $\delta$  of either the Raman or the rf fields shifts the energies of the  $m_F = \pm 1$  states. Raman transitions are two-photon, exciting up to a virtual state and coming back down to an adjacent hyperfine state, with an accompanying momentum transfer. Rf couples adjacent hyperfine states directly. Figure taken from ref. [2]

or for any value of  $F$

$$H_{\text{rf}} = H_{\text{KE}} + \hbar\delta F_z + \hbar\epsilon F_z^2 + \Omega F_x/2. \quad (2.29)$$

The band structure of this Hamiltonian can be seen in Figure 8, where we have diagonalized Eq. 2.28 for a range of momenta  $k_x$  (we have isolated  $k_x$  for comparison with Raman coupling, as will be seen in the next section). The parabolas are simply the free particle dispersion relations along one dimension, with three bands arising from the three available spin states. It is convenient to define the magnetization of an eigenstate  $m = \sum_{m_F} m_F * p_{m_F}$ , where  $p_{m_F}$  is the fractional population in the  $m_F$  state. We have indicated the magnetization of the eigentate by coloring the

eigenenergies, with  $m = -1$  in red,  $m = 0$  in green, and  $m = +1$  in blue. In Figure 8a, both the detuning and the coupling strength are zero. Therefore, there are simply three free particle dispersions, each exactly correlated with a particular spin state, the  $m_F = \pm 1$  are degenerate and the  $m_F = 0$  state is slightly offset by the quadratic shift  $\hbar\epsilon$ . In Figure 8c, the coupling strength is again zero, but the detuning has been turned on, lifting the degeneracy between the  $m_F = \pm 1$  states. Figure 8b,d shows the same conditions as a,c, respectively, but with the coupling strength turned on. In Figure 8b, where the detuning is zero and the quadratic shift is negligible compared to the coupling strength, all states average to a magnetization of zero—the  $m_F = \pm 1$  states are symmetrically populated. In Figure 8d, this symmetry is broken by the presence of a detuning.

### 2.4.3 Raman coupling Hamiltonian

The counter-propagating Raman beams, as seen in Figure 7, couple the same states as the rf. They do so via the vector light shift created by the pair of beams. The electric field due to the right going beam (red in Figure 7a) is  $\mathbf{E} = E_0 \exp(ik_R x - i\omega t) \mathbf{e}_y$ , where  $E_0$  is the amplitude of the electric field and  $\hbar k_R = h/\lambda_R = \hbar\omega/c$ . The electric field from the left going beam (gray in Figure 7b) is  $\mathbf{E} = E_0 \exp(-ik_R x - i(\omega + \Delta\omega)t) \mathbf{e}_z$ . This combines to give an effective field from the vector light shift [7]  $B_{\text{eff}} \propto \mathbf{E} \times \mathbf{E}^* \propto -E_0^2 \cos(2k_R x + \Delta\omega t) \mathbf{e}_x$ . Going through the same procedure as for the rf coupling case, including the transfer into the rotating frame and the rotating wave approximation, we obtain the same Hamiltonian in the basis of bare spin states  $| -1 \rangle, | 0 \rangle, | 1 \rangle$  but with an extra phase factor:

$$H_{\text{Raman}} = H_{\text{KE}} + \hbar \begin{pmatrix} \delta & \Omega/2 e^{-i2k_R x} & 0 \\ \Omega/2 e^{i2k_R x} & -\epsilon & \Omega/2 e^{-i2k_R x} \\ 0 & \Omega/2 e^{i2k_R x} & -\delta \end{pmatrix}, \quad (2.30)$$



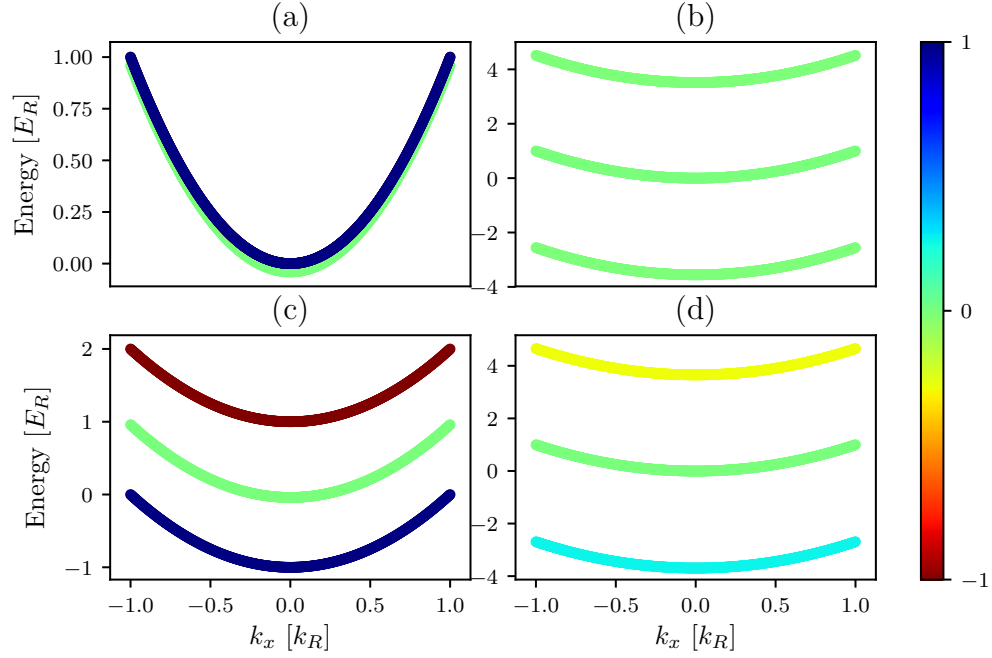


Figure 8: Band structure of the rf Hamiltonian, Eq. 2.28, in momentum space. For all plots, the quadratic Zeeman shift  $\hbar\epsilon = 0.04E_R$ , and the color represents magnetization, labeled by the colorbar. (a)  $\hbar\Omega = 0$ ,  $\hbar\delta = 0$ . No coupling or detuning is present, so the only separation between the bands is due to the quadratic shift  $\hbar\epsilon$ . (b)  $\hbar\Omega = 5.0E_R$ ,  $\hbar\delta = 0$ . (c)  $\hbar\Omega = 0$ ,  $\hbar\delta = 1.0E_R$ . Even though the coupling strength is zero, the bands are separated by the detuning. (d)  $\hbar\Omega = 5.0E_R$ ,  $\hbar\delta = 1.0E_R$ .

where  $\delta = \omega_z - \Delta\omega$ .

This phase difference between the rf and Raman Hamiltonian has an intuitive physical explanation. In order to undergo a Raman transition, an atom first absorbs a photon from one beam, getting a momentum kick equal to the recoil momentum  $\hbar k_R$ . Then, to decay back down to an adjacent spin state, the undergoes stimulated emission into the field of the other (counter-propagating) beam, acquiring another recoil momentum kick in the same direction for a total of  $2\hbar k_R \mathbf{e}_x$ . Therefore, the Raman coupling Hamiltonian for  $F = 1$ , after transforming into the rotating frame and performing the rotating wave approximation, can be written in the same way as the rf Hamiltonian in Eq. 2.28 with the addition of a momentum kick—in real space, an aquired phase—of  $e^{i2k_R x}$ .

We can again make a basis transformation to get rid of this phase. Let us define  $|-1\rangle' = \exp(-2ik_R x) |-1\rangle = |k_x - 2k_R, -1\rangle$ ,  $|0\rangle' = |0\rangle = |k_x, 0\rangle$ ,  $|1\rangle' = \exp(2ik_R x) |1\rangle = |k_x + 2k_R, 1\rangle$ , where for third definition we went into the momentum basis and labelled the states by a combination of their momentum and spin state. Then, including the kinetic energy term along  $\mathbf{e}_x$  explicitly, we obtain the Hamiltonian in the new basis as:

$$H_{\text{Raman}} = H_{\text{KE}}^{(y,z)} + \begin{pmatrix} \frac{\hbar^2(k_x - 2k_R)^2}{2m} + \hbar\delta & \hbar\Omega/2 & 0 \\ \hbar\Omega/2 & \frac{\hbar^2 k_x^2}{2m} - \hbar\epsilon & \hbar\Omega/2 \\ 0 & \hbar\Omega/2 & \frac{\hbar^2(k_x + 2k_R)^2}{2m} - \hbar\delta \end{pmatrix}. \quad (2.31)$$

It is convenient to define the Raman recoil energy as  $E_R = \frac{\hbar^2 k_R^2}{2m}$ . The band structure of this Hamiltonian is shown in Figure 9, for several representative parameter values, with the magnetization labelled by the color. Figure 9a shows the band structure in the limit of zero coupling and zero detuning, but where we have already gone into the basis  $|k_x - 2k_R, -1\rangle, |k_x, 0\rangle, |k_x + 2k_R, 1\rangle$ ; therefore, the free particle parabola corresponding to the  $m_F = 1$  spin states is shifted to center on

$k_x = -2k_R$  and the  $m_F = -1$  parabola is shifted to center on  $k_x = 2k_R$ . As the coupling is turned on to  $\hbar\Omega = 1E_R$  in Figure 9b, the points where the parabolas cross become 'avoided crossings', separating into three bands where magnetization (and the underlying spin distribution) depends on the momentum  $k_x$ . As the coupling strength is turned up even further to  $\hbar\Omega = 5E_R$  in Figure 9c, the lowest band goes from having three minima, one corresponding to each original spin state, to only one minimum. This transition happens at  $\hbar\Omega = 4E_R$  [6]. In Figure 9d, we show the band structure again in the limit of zero coupling, but this time with a detuning of  $\hbar\delta = 1.0E_R$ . Note that the detuning tips the parabolas with respect to each other. Figure 9e shows the detuned system with coupling strength turned up to  $\hbar\Omega = 1E_R$ , still in the three minima regime but with avoided crossings creating three momentum and spin coupled bands. In Figure 9f, the detuned system is turned up to a coupling strength of  $\hbar\Omega = 5E_R$ , creating a single minimum, this time offset from  $k_x = 0$ .

We can write the general  $F$  version of the Raman coupled Hamiltonian in the basis  $|k_x + m_F * 2k_R, m_F\rangle$ , where  $-F \leq m_F \leq F$ , as:

$$H_{\text{Raman}} = H_{\text{KE}}^{(y,z)} + \hbar^2(k_x\mathcal{I} + 2k_R F_z)^2/2m + \hbar\delta F_z + \hbar\epsilon F_z^2 + \Omega F_x/2. \quad (2.32)$$

#### 2.4.4 Calibration of Raman and Rf dressed states

To calibrate the rf and Raman coupling strengths, we take a similar approach to the 1-D lattice calibration: start in a pure spin state, for example  $m_F = 0$ , and turn the coupling on non-adiabatically to induce Rabi oscillations between the coupled states. Then, during time-of-flight, apply a Stern-Gerlach gradient pulse to separate the spin components and observe the fractional populations in different spin states as a function of Rabi oscillation time.

Figure 10a,b shows example images obtained in time-of-flight when pulsing on

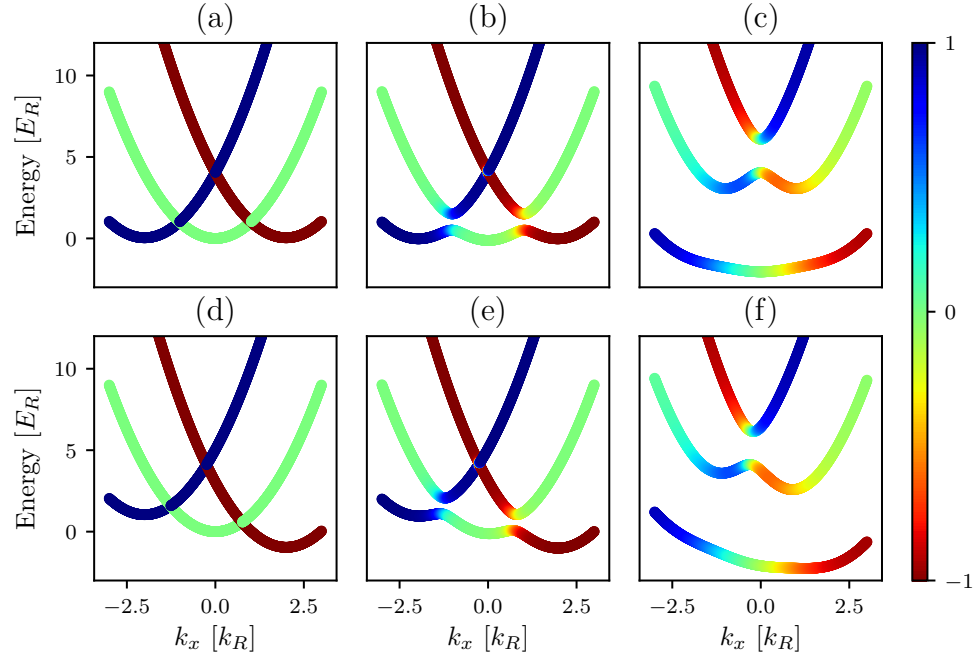


Figure 9: Band structure of the Raman Hamiltonian, Eq. 2.31, in momentum space. For all plots, the quadratic Zeeman shift  $\hbar\epsilon = 0.04E_R$ , and the color represents magnetization, labeled by the colorbar. (a)  $\hbar\Omega = 0$ ,  $\hbar\delta = 0$ . (b)  $\hbar\Omega = 1.0E_R$ ,  $\hbar\delta = 0$ . (c)  $\hbar\Omega = 5.0E_R$ ,  $\hbar\delta = 0$ . (d)  $\hbar\Omega = 0.0$ ,  $\hbar\delta = 1.0E_R$ . (e)  $\hbar\Omega = 1.0E_R$ ,  $\hbar\delta = 1.0E_R$ . (f)  $\hbar\Omega = 5.0E_R$ ,  $\hbar\delta = 1.0E_R$

an rf coupling field for atoms in the  $F = 1$  and  $F = 2$  manifold, respectively. The Stern-Gerlach gradient pulse separates the spin components along the horizontal axis in the images. The fractional population in each state can then be obtained by summing up the optical depth in each cloud and dividing by the total optical depth. Similarly, Figure 11a shows an example time-of-flight image obtained when pulsing on a Raman coupling field on an  $F = 1$  cloud initially in the  $m_F = 0$  spin state. Here, the spin states are separated along the horizontal axis by the same Stern-Gerlach pulse. In addition, the recoil momentum obtained when undergoing a Raman transition separates the different spin states along the vertical axis—parallel to the Raman beams along  $\mathbf{e}_x$ . The direction of the Stern-Gerlach gradient was chosen purposefully to be perpendicular to the Raman direction  $\mathbf{e}_x$  for easy separation of the two effects.

These population oscillations can then be fit for coupling strength  $\hbar\Omega$  and detuning  $\hbar\delta$ . Note that the quadratic Zeeman shift  $\hbar\epsilon$  is set by the strength of the bias field  $B_0$  and therefore often well known - we do not fit for this. The theoretic predictions are obtained by applying the time evolution operator  $U = \exp(-iH_{\text{Raman/rf}}t/\hbar)$  to an initial state  $\Psi$  in the appropriate basis. Figure 10c shows an example time series of rf pulsing in the  $F = 1$  manifold, starting in the  $m_F = 0$  state. The lines of best fit are overlayed on experimental data, extracting fit parameters  $\hbar\Omega = 0.863 \pm 0.004E_R$  and  $\hbar\delta = -0.198 \pm 0.007E_R$ . Figure 10d shows an example time series of rf pulsing in the  $F = 2$  manifold, starting in the  $m_F = -2$  state. Here, the extracted fit parameters were  $\hbar\Omega = 1.000 \pm 0.002E_R$  and  $\hbar\delta = -0.061 \pm 0.001E_R$ .

Figure 11b shows an example time series of Raman pulsing in the  $F = 1$  manifold, starting in the  $m_F = 0$  state, with fitted parameters  $\hbar\Omega = 1.47 \pm 0.01E_R$  and  $\hbar\delta = 0.004 \pm 0.024E_R$ . Note that although the coupling strength is almost double the rf coupling strength in Figure 10c, the contrast (peak to peak oscillation

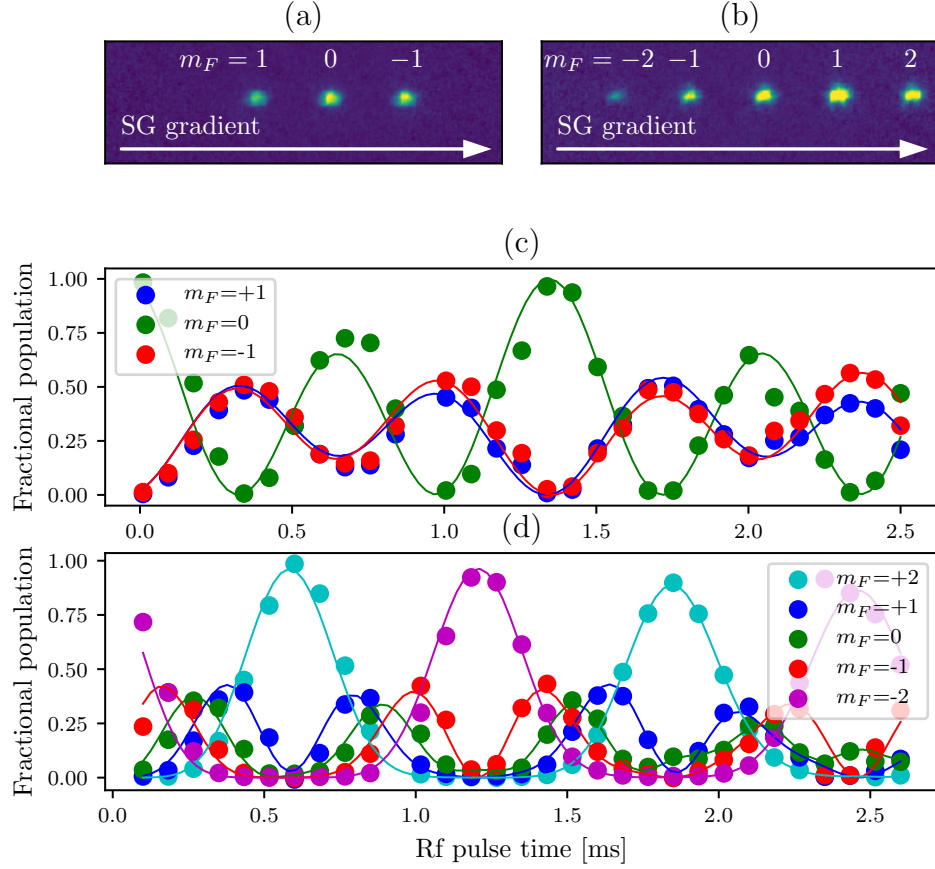


Figure 10: Pulsing on rf coupling. (a) Example time-of-flight image during an rf pulsing experiment in the  $F = 1$  manifold. Spin states are separated via a Stern-Gerlach pulse along the horizontal direction. (b) Example time-of-flight image during an rf pulsing experiment in the  $F = 2$  manifold. Here, 5 spin components are present. (c) Pulsing experiment in the  $F = 1$  manifold. Dots represent fractional populations in different spin states measured from time-of-flight images, and lines represent best fit theory curves. Fitted parameters are  $\hbar\Omega = 0.863 \pm 0.004E_R$ ,  $\hbar\delta = -0.198 \pm 0.007E_R$ . (d) Pulsing experiment in the  $F = 2$  manifold. Dots represent fractional populations in different spin states measured from time-of-flight images, and lines represent best fit theory curves. Fitted parameters are  $\hbar\Omega = 1.000 \pm 0.002E_R$ ,  $\hbar\delta = -0.061 \pm 0.001E_R$ .  $\hbar\epsilon = 0.038E_R$  for all panels.

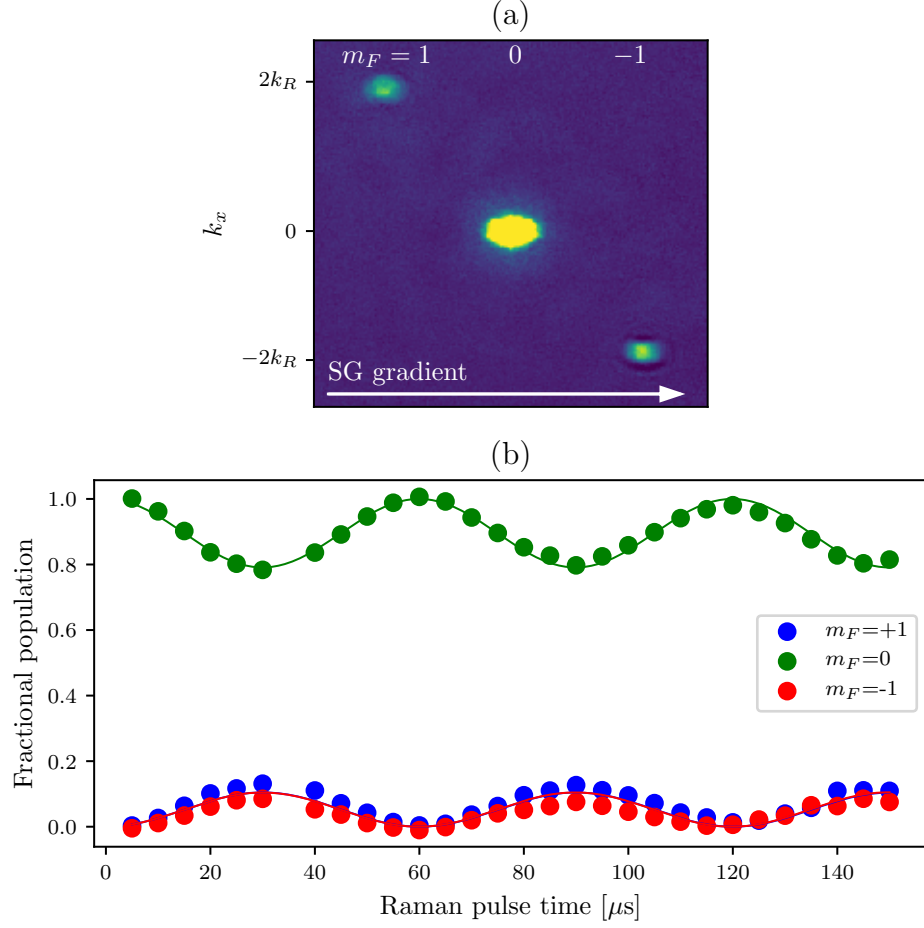


Figure 11: Pulsing on Raman coupling. (a) Example time-of-flight image during a Raman pulsing experiment in the  $F = 1$  manifold. A Stern-Gerlach pulse during time-of-flight separates different spin components along the horizontal direction, and different momentum orders fly apart along the vertical direction. (b) Fractional population in different spin states during a Raman pulsing experiment as a function of time. Dots represent data and lines represent a best fit from theory. The fitted parameters are  $\hbar\Omega = 1.47 \pm 0.01 E_R$ ,  $\hbar\delta = 0.004 \pm 0.024 E_R$ . The quadratic Zeeman shift was  $\hbar\epsilon = 0.038 E_R$ .

of the fractional population in, say, the  $mF = 0$  state) is much lower in the Raman data than in the rf. This is a direct consequence of the recoil momentum transfer, and can be understood by looking at the band structure. For rf, the coupled bands at initial momentum  $k_x = 0$  are separated by the coupling strength, see Figure ??b. For Raman, even at zero coupling strength, due to the shifting of the parabolas by  $2k_R$ , and  $k_x = 0$  the higher bands are  $\hbar^2(2k_R)^2/2m = 4E_R$  separated from the lower bands. Therefore, the energy difference is larger and the fraction in the excited band will be lower, leading to lower contrast.



## Chapter 6: Synthetic Magnetic Fields in Synthetic Dimensions

In condensed matter, 2-D systems in high fields have proved to be of great technological use and scientific interest. The integer quantum Hall effect (IQHE) [8], with its quantized Hall resistance, had given rise to an ultra-precise standard for resistivity. It was also one of the first examples of topology playing an important role in physics—the precise quantization of the Hall conductance is guaranteed by the non-trivial topology of the system [9]. This quantizes the magnetic flux into flux quanta of  $\Phi_0 = 2\pi\hbar/e$ , where  $e$  is the electron charge, and leads to a new ‘plateau’ in the resistivity when an additional quantum of flux is threaded through the system.

In the IQHE system, the underlying lattice structure of metal is effectively washed out—the magnetic flux per individual lattice plaquette is negligible. However, new physics arises when the magnetic flux per plaquette is increased to some non-negligible fraction of the flux quantum, giving rise to the Hofstadter butterfly [10]. These regimes are hard to reach experimentally, since the typical plaquette size in crystalline material is of order a square angstrom, and the magnetic field necessary to thread create a magnetic flux of  $\Phi_0$  through such a narrow area is of order  $\approx 10^4$  Tesla, not accessible with current technology.

Several platforms have, however, reached the Hofstadter regime by engineering systems with large effective plaquette size, in engineered materials [11, 12], and in atomic [13–18] and optical [19] settings. Here, we use the approach of synthetic dimensions [20] to reach the Hofstadter regime. We demonstrate the non-trivial topology of the system created, and use it to image skipping orbits at the edge of

the 2-D system—a hallmark of 2-D electron systems in a semiclassical treatment.

The work described in this chapter was published in [21].

## 6.1 Synthetic dimensions setup

Any internal degree of freedom can be thought of as a synthetic dimension—the different internal states can be treated as sites along this synthetic direction. As long as there is some sense of distance along this direction, i.e. some of the internal states are 'nearest neighbors' while others are not, this is a meaningful treatment. In our case an effective 2-D lattice is formed by sites formed by a 1-D optical lattice along a 'real' direction, here  $\mathbf{e}_x$ , and the atom's spin states forming sites along a 'synthetic' direction,  $\mathbf{e}_s$ .

The experimental setup for this system is schematically represented in 1a. The BEC is subject to a 1-D optical lattice, formed by a retro-reflected beam of  $\lambda_L = 1064nm$  along  $\mathbf{e}_x$ . A bias magnetic field  $B_0$  along  $\mathbf{e}_z$  separates the different spin states. The spin states can be thought of as sites along a synthetic dimension even without any coupling field. However, only once a coupling field is present do they acquire a sense of distance. We couple them via rf or Raman coupling, which only couples adjacent spin states. The Raman beams illuminating the atoms are along the same  $\mathbf{e}_x$  direction as the 1-D optical lattice. The rf field has components both along the  $\mathbf{e}_x$  and  $\mathbf{e}_y$ .

Figure 1b sketches out the effective 2-D lattice created. Here, we have labelled the lattice sites along the 'real' direction  $\mathbf{e}_x$  by site index  $j$ . In the tight binding approximation, we can describe a lattice hopping between adjacent sites with tunneling amplitude  $t_x$ . Similarly, the sites along the 'synthetic' dimension are labelled by site index  $m$  (identical to spin projection quantum number  $m_F$ ), and the rf or Raman coupling here plays the role of a tunneling amplitude  $t_s$ . In the case of rf coupling, there is no momentum kick associated with spin exchange, and both  $t_x$

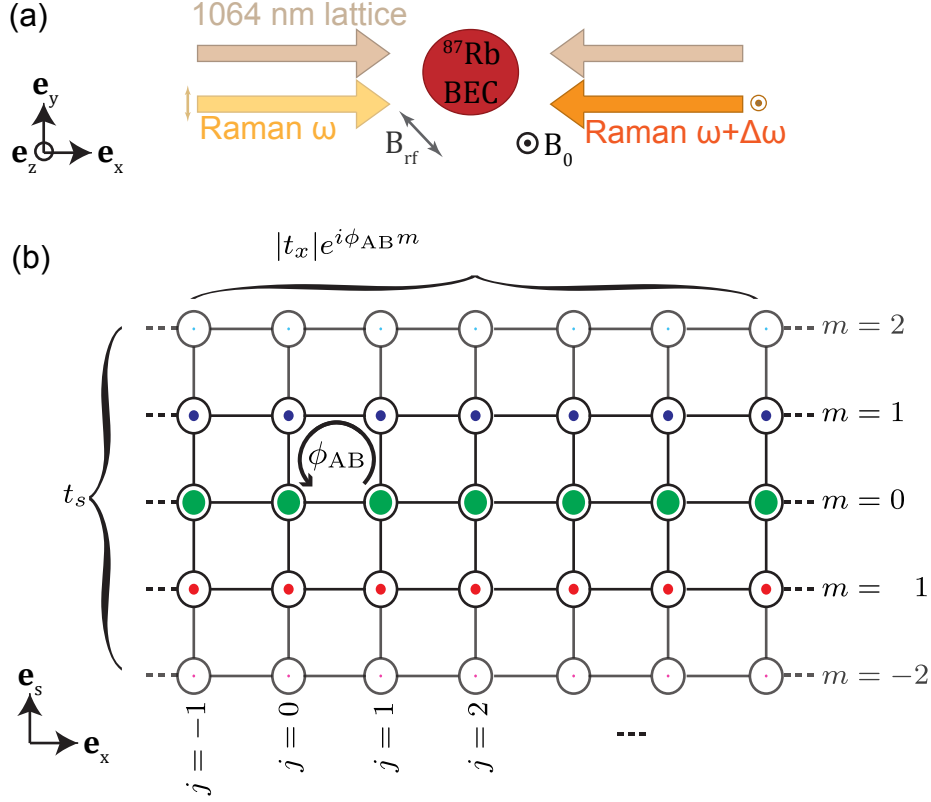


Figure 1: Setup of effective 2-D lattice. (a) Beam geometry. The BEC is subject to a bias magnetic field  $B_0$  in the  $\mathbf{e}_z$  direction. The 1-D lattice beam and Raman beams are both along the  $\mathbf{e}_x$  direction, and the rf field can be applied with projections onto both the  $\mathbf{e}_x$  and  $\mathbf{e}_y$ . (b) Schematic of the effective 2-D lattice. Sites along  $\mathbf{e}_x$  are formed by the 1-D optical lattice and labelled by site number  $j$ . Sites along the synthetic direction  $\mathbf{e}_s$  are formed by the spin states: 3 sites for atoms in the  $F = 1$  manifold and 5 sites for atoms in  $F = 2$ . These sites are labelled by  $m$ . Raman transitions induce a phase shift, which can be gauge transformed into a tunneling phase along the  $\mathbf{e}_x$  direction. This leads to a net phase when hopping around a single lattice plaquette of  $\phi_{AB}$ .

and  $t_s$  are real.

In the case of Raman coupling, however, there is a momentum kick of  $2k_R$  associated with every spin transfer, and therefore a phase factor of  $\exp(2ik_R x)$  with every spin 'tunneling' event. Since position  $x$  is set by the 1-D lattice,  $x_j = j\lambda_L/2 = j\pi/k_L$ , and the space dependent phase factor is  $\exp(2\pi i k_R/k_L j)$ . An absolute phase change in the wavefunction is not meaningful. However, a phase acquired when going around a plaquette and coming back to the same place is meaningful, as one could imagine one atom staying at the same site and the other going around a plaquette and coming back to detect the phase difference. In this setup, the phases acquired while going around a single plaquette are, starting at some lattice site  $|j, m\rangle$ , are: 0 (for tunneling right to  $|j+1, m\rangle$ ),  $2\pi i k_R/k_L(j+1)$  (for tunneling up to  $|j+1, m+1\rangle$ ), 0 (for tunneling left to  $|j, m+1\rangle$ ) and  $-2\pi i k_R/k_L j$  (for tunneling back down to  $|j, m\rangle$ ). The total phase acquired is thus  $\phi_{AB} = 2\pi k_R/k_L$ , independent of the starting lattice site. Since the absolute phase does not matter and only the value of  $\phi_{AB}$ , we can perform a phase transformation that shifts the tunneling phase onto the spatial direction, defining  $t_x = |t_x|\exp(i\phi_{AB}m)$  and  $t_s = |t_s|$ , as labelled in Figure 1b.

To see how this phase implies an effective magnetic field, we draw an analogy to the Aharonov-Bohm effect [22, 23] from quantum mechanics. In this effect, consider an infinite solenoid with an electric current running through it. The magnetic field  $B$  in this setup exists only inside the solenoid, while the magnetic vector potential persists outside the solenoid. However, if two electrons are sent on a trajectory around the solenoid, even though they never pass through any magnetic field, they nevertheless acquire a relative phase that can be detected by interfering them with each other. This relative phase is given by  $\phi_{AB} = 2\pi\Phi/\Phi_0$ , where  $\Phi = B * A$  is the magnetic flux through the solenoid ( $A$  is the area pierced by the magnetic field) and  $\Phi_0 = h/e$  is the flux quantum, with  $e$  the electron charge. Since in our system,

the atoms acquire a phase when they perform a closed loop around a single lattice plaquette. Therefore, they behave as though there was an infinite solenoid piercing each plaquette with a magnetic field going through it, and the flux per plaquette in units of the flux quantum is  $\Phi/\Phi_0 = \phi_{AB}/2\pi = k_R/k_L$ . For the case of rf coupling, the phase acquired at every transition is 0 and the fluxss  $\Phi/\Phi_0 = 0$ .

## 6.2 Hamiltonian of the effective 2-D system

### 6.2.1 Hamiltonian

The full Hamiltonian of this system, without making the tight binding approximation, can be written down by combining the lattice Hamiltonian (eqn. 2.17) and the rf (eqn. 2.28) or Raman Hamiltonian (eqn. 2.31). To do this, we write a new basis that encompasses both the momentum and the spin degrees of freedom. For the lattice Hamiltonian, we used the momentum basis

$$\begin{pmatrix} \vdots \\ |q + 4k_L\rangle \\ |q + 2k_L\rangle \\ |q\rangle \\ |q - 2k_L\rangle \\ |q - 4k_L\rangle \\ \vdots \end{pmatrix}. \quad (6.1)$$

For the Raman Hamiltonian in the  $F = 1$  manifold, we used the spin and momentum basis

$$\begin{pmatrix} |k_x - 2k_R, -1\rangle \\ |k_x, 0\rangle \\ |k_x + 2k_R, 1\rangle \end{pmatrix}. \quad (6.2)$$

In a lattice, the momentum  $k_x$  becomes crystal momentum  $q$ . For every state in the lattice basis, we now expand to three states, one for each spin state, with the appropriate momentum shifts. We obtain

$$\begin{pmatrix} \vdots \\ |q + 2k_L - 2k_R, -1\rangle \\ |q + 2k_L, 0\rangle \\ |q + 2k_L + 2k_R, 1\rangle \\ |q - 2k_R, -1\rangle \\ |q, 0\rangle \\ |q + 2k_R, 1\rangle \\ |q - 2k_L - 2k_R, -1\rangle \\ |q - 2k_L, 0\rangle \\ |q - 2k_L + 2k_R, 1\rangle \\ \vdots \end{pmatrix}. \quad (6.3)$$

In this basis, we combine the lattice and Raman Hamiltonians (ommiting the kinetic energy in the other two directions) in an infinite block matrix form as

$$H = \begin{pmatrix} \ddots & & & \\ & \mathbf{H}_{\mathbf{R}}(2k_L) & \frac{\mathbf{V}_0}{4} & \mathbf{0} \\ & \frac{\mathbf{V}_0}{4} & \mathbf{H}_{\mathbf{R}}(0) & \frac{\mathbf{V}_0}{4} \\ & \mathbf{0} & \frac{\mathbf{V}_0}{4} & \mathbf{H}_{\mathbf{R}}(-2k_L) \\ & & & \ddots \end{pmatrix}, \quad (6.4)$$

where  $\mathbf{H}_R(x)$  is the Raman Hamiltonian with a momentum shift of  $x$ :

$$\mathbf{H}_R(n2k_L) = \begin{pmatrix} \frac{\hbar^2(q+n2k_L-2k_R)^2}{2m} + \hbar\delta & \hbar\Omega/2 & 0 \\ \hbar\Omega/2 & \frac{\hbar^2(q+n2k_L)^2}{2m} - \hbar\epsilon & \hbar\Omega/2 \\ 0 & \hbar\Omega/2 & \frac{\hbar^2(q+n2k_L+2k_R)^2}{2m} - \hbar\delta \end{pmatrix}, \quad (6.5)$$

the matrix  $\frac{\mathbf{V}_0}{4}$  is a 3x3 diagonal matrix lattice coupling strength  $\frac{V_0}{4}$  on the diagonal, and  $\mathbf{0}$  is a 3x3 matrix of zeros. This extends in both directions with  $\mathbf{H}_R(2nk_L)$  on the diagonal blocks and  $\frac{\mathbf{V}_0}{4}$  as the first off-diagonal blocks and  $\mathbf{0}$  everywhere else.

This Hamiltonian is easily extended to higher  $F$  values by replacing the Raman blocks  $\mathbf{H}_R(x)$  with the corresponding Raman coupling Hamiltonian from eqn. 2.32, and extending the diagonal matrix  $\frac{\mathbf{V}_0}{4}$  and the zero matrix  $\mathbf{0}$  to be  $(2F+1) \times (2F+1)$ .

For computational convenience, we convert to lattice recoil units,  $E_L = \hbar^2 k_L^2 / 2m$ ,  $k_L = 2\pi/\lambda_L$ . Then the diagonal blocks become

$$\mathbf{H}_R(n)/E_L = \begin{pmatrix} (q+n-\phi_{AB}/2\pi)^2 + \hbar\delta & \hbar\Omega/2 & 0 \\ \hbar\Omega/2 & (q+n)^2 - \hbar\epsilon & \hbar\Omega/2 \\ 0 & \hbar\Omega/2 & (q+n+\phi_{AB}/2\pi)^2 - \hbar\delta \end{pmatrix}, \quad (6.6)$$

where  $\hbar\delta$ ,  $\hbar\Omega$  and  $\hbar\epsilon$  are now written in units of  $E_L$ ,  $q$  is written in units of  $k_L$  and we have used the fact that  $\phi_{AB}/2\pi = k_R/k_L$ . The off-diagonal blocks  $\frac{\mathbf{V}_0}{4}$  will be the same 3x3 diagonal matrices, with  $\frac{V_0}{4}$  in units of  $E_L$ .

## 6.2.2 Band structure

The band structure of this Hamiltonian is presented in Figure 2. Here, we have restricted ourselves to the lowest lattice band. We can do this because the energy splitting between the lowest and second lowest lattice band is of order  $4E_L$  (see Figure 2), while the width of the lowest band, given by the amplitude of the

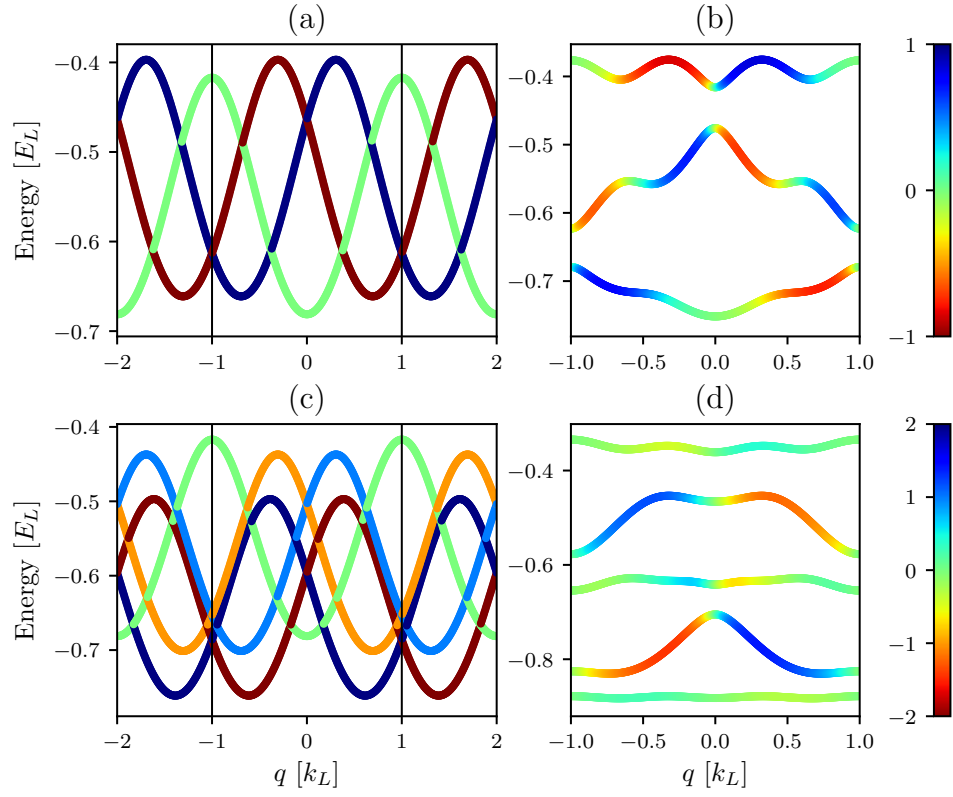


Figure 2: Band structure of the synthetic dimensions Hamiltonian, eqn. 6.4. For all panels, the detuning  $\hbar\delta = 0$  and the quadratic shift  $\hbar\epsilon = 0.02E_L$ . (a)  $F = 1$ ,  $\hbar\Omega = 0.0$ . (b)  $F = 1$ ,  $\hbar\Omega = 0.5$ . (c)  $F = 2$ ,  $\hbar\Omega = 0.0$ . (d)  $F = 2$ ,  $\hbar\Omega = 0.5$ .



approximate sinusoid, is of order  $0.3E_L$  for our range of lattice depths, around  $5.0E_L$ . As long as the Raman coupling stays small compared to the lattice band spacing, the higher lattice bands are energetically separated enough that they can be ignored.

Therefore, we can think of the Raman coupling analogously to the free space Raman coupling (see section 2.4.3), except instead of free space parabolas each spin state gets a lowest lattice band sinusoid. Figure 2a shows this in the limit of no Raman coupling,  $\Omega = 0$ , but with the lattice on at  $V_0 = 4.0E_L$ . The quadratic Zeeman shift is  $\hbar\epsilon = 0.02E_L$  and the detuning  $\delta = 0$ . The  $m_F = -1$  sinusoid is shifted  $2k_R$ , similarly to section 2.4.3, but since the sinusoid is periodic with  $2k_L$ , it folds into the first Brillouin zone of the lattice, such that the nearest minimum to  $q = 0$  is at  $q = 2k_R - 2k_L = (2\phi_{AB}/2\pi - 2)k_L$ . The edges of the Brillouin zone are marked by horizontal lines. The color indicates magnetization  $\langle m \rangle = \sum_{m_F} m_F n_{m_F}$ , where  $n_{m_F}$  is the fractional population in the  $m_F$  state. In synthetic dimensions language,  $\langle m \rangle$  is the expectation value of position along  $\mathbf{e}_s$ .

In Figure 2b, we have restricted ourselves to the first Brillouin zone and turned on the Raman coupling to  $\hbar\Omega = 0.5E_L$ . The crossings of the bands in Figure 2a become avoided crossings, and the lowest band now has a spin dependence on crystal momentum. Figure 2c-d shows the same progression for the  $F = 2$  manifold. Figure 2c is taken in the limit of  $\hbar\Omega = 0.0$ . All of the 5 spin states get 'folded' back into the first Brillouin zone due to the lattice periodicity of the bands. The different heights of the sinusoids are due to the quadratic Zeeman shift  $\hbar\epsilon = 0.02E_L$ . The lattice depth is again  $V_0 = 5.0E_L$  and detuning  $\hbar\delta = 0$ . In Figure 2d we have restricted ourselves to the first Brillouin zone and turned on the Raman coupling to  $\hbar\Omega = 0.5E_L$ . Note that the inverted hyperfine structure in 2c (meaning that the quadratic shift pushed the  $m_F = 0$  state up rather than down in energy compared to the others), combined with the Raman coupling serves to make the lowest band in the  $F = 2$  manifold close to flat.

### 6.2.3 Calibration

To calibrate the lattice depth  $V_0$  in the synthetic dimensions system, we can simply calibrate the lattice depth without Raman or rf coupling as described in Section 2.3.4. However, we are operating at very low Raman coupling strengths,  $\hbar\Omega \approx 0.5E_L$ . This is necessary because in the synthetic dimensional system the Raman coupling plays the role of tunneling, which has to be small to approximate the tight binding limit. At these low Raman couplings, simple pulsing as described in Section 2.4.4, as the contrast of the Rabi oscillations would be too low to resolve. Therefore, we calibrate the Raman coupling and detuning with the full synthetic dimensions system, where the 'folding in' effect of the lattice makes the higher Raman bands much closer energetically than without the lattice, leading to larger contrast and allowing for accurate calibration.

To do this, we must first adiabatically load the lowest 1-D lattice band. To do that, we must ramp on the lattice potential on a time scale slow compared to the band spacing,  $\approx 4E_L$ . This gives  $t \approx h/4E_L = 0.12$  ms. Figure 3a shows the full ramping scheme. We ramp the lattice on in  $\approx 20$  ms. Then, we must pulse on the Raman coupling on a time scale fast compared to the spin sub-band level spacing to produce Rabi oscillations, but still adiabatic with respect to the lattice spacing to avoid exciting to the higher lattice band. We ramp the Raman beams on in  $300 \mu\text{s}$ . Then, the system is held on for a variable amount of time before all light is snapped off and the atoms are allowed to expand in time-of-flight. For the case of  $F = 2$  atoms, the transfer to the  $F = 2$  manifold is done in the 1-D lattice before the Raman beams are ramped on to minimize the time spend in the  $F = 2$  manifold.

Figure 3c,d shows sample time-of-flight images during the calibration procedure for  $F = 1$  and  $F = 2$  respectively. The vertical axis is  $\mathbf{e}_x$ , aligned with the

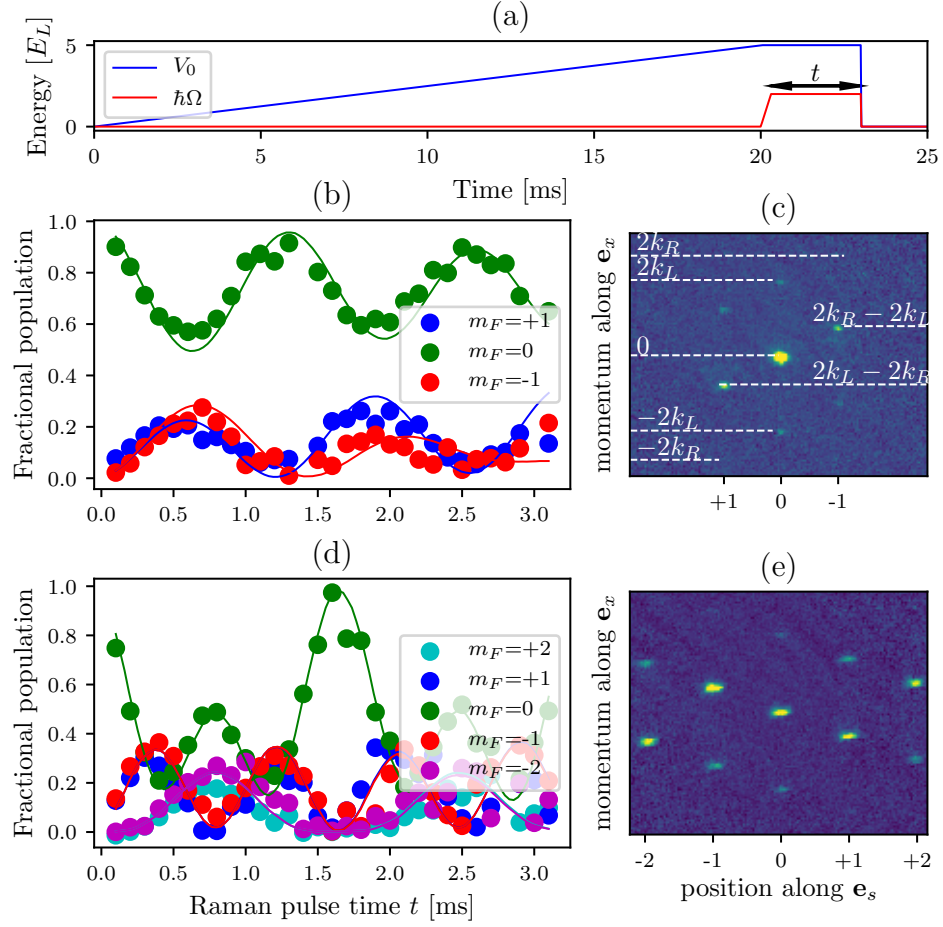


Figure 3: Calibration of synthetic dimensions lattice. (a) Ramping procedure. The blue line represents the 1-D lattice depth as a function of time and the red line represents Raman coupling as a function of time. Both are held on for a variable amount of time  $t$ , producing Rabi oscillations. (b) Example of fractional populations in different  $m$  states as a function of time  $t$  in the  $F = 1$  manifold. Dots indicate data and lines indicate the best fit to theory, with parameters  $\hbar\Omega = 0.56 \pm 0.01 E_L$  and  $\hbar\delta = 0.029 \pm 0.002 E_L$ . (c) Example time-of-flight image in the  $F = 1$  manifold. A Stern-Gerlach gradient pulse separates different  $m$  states along the horizontal axis, while the lattice and Raman beams give momentum along the vertical axis. (d) Example of fractional populations in different  $m$  states as a function of time  $t$  in the  $F = 2$  manifold. Dots indicate data and lines indicate the best fit to theory, with parameters  $\hbar\Omega = 0.61 \pm 0.002 E_L$  and  $\hbar\delta = 0.002 \pm 0.001 E_L$ . (e) Example time-of-flight image in the  $F = 2$  manifold. A Stern-Gerlach gradient pulse separates different  $m$  states along the horizontal axis, while the lattice and Raman beams give momentum along the vertical axis.

lattice and Raman beams. Since the atoms have expanded in time-of-flight, this axis corresponds to the momentum  $k_x$ . The horizontal axis of the image is the axis along which a Stern-Gerlach magnetic field gradient, separating the different spin states, is applied. Therefore, this axis is the position  $m$  along the synthetic dimension  $\mathbf{e}_s$ . In the effectively 2-D synthetic dimensions lattice language, this is a 'hybrid' imaging technique—imaging momentum along one lattice direction and position along the other.

Figure 3c labels some notable momentum orders. The central order is at  $k_x = 0$ , where the atoms start before the experiment. Two higher lattice orders, at  $k_x = \pm 2k_L$ , are populated for the same spin  $m = 0$ .  $k_x = \pm 2k_R$  is labelled, but not visibly populated, to indicate where the orders would appear if only Raman coupling was present with a higher coupling strength. Due to the 'folding in' effect of the lattice, the brightest orders of the  $m = \pm 1$  states appear at  $k_x = \pm(2k_L - 2k_R)$ . The  $F = 2$  states follow the same pattern, not labelled in Figure 3e as there are too many orders.

For each value of the time  $t$  we sum up the total optical depth in all of the orders of each spin state to obtain fractional populations for each spin state as a function of time. An example scan in the  $F = 1$  manifold is shown in Figure 3b. The colored dots represent the data for different spin states, and the lines represent the best fit to theory. Here, the significant detuning makes populations in the  $m = \pm 1$  states unequal. An example scan in the  $F = 2$  manifold is shown in Figure 3e. Here, the detuning is small and states with opposite spin oscillate in approximate unison.

### 6.2.4 Tight binding approximation

The synthetic dimensions Hamiltonian can be approximated in the tight binding limit as:

$$H = - \sum_{j,m} t_x e^{i\phi_{AB}m} |j+1, m\rangle \langle j, m| + t_s(m) |j, m+1\rangle \langle j, m| + A_m |j, m\rangle \langle j, m| + h.c., \quad (6.7)$$

where  $j$  and  $m$  label sites along  $\mathbf{e}_x$  and  $\mathbf{e}_s$  respectively, as shown in Figure 1b.  $t_s = |t_s|$  and  $t_x = |t_x| \exp(-i\phi_{AB}m)$  are the associated tunnelings.  $A_m$  captures the spin dependent diagonal elements, detuning  $\hbar\delta$  and quadratic shift  $\hbar\epsilon$ . Here, we have implicitly restricted ourselves to the lowest 1-D lattice band, and assumed that tight binding, ie confinement at discrete lattice sites, is a good approximation (see 2.3.3).  $t_s$  is not a spin dependent quantity for  $F = 1$  atoms, but is for  $F = 2$ , where differences in Clebsch-Gordan coefficients create non-uniform tunneling. In the limit of zero detuning and neglecting the quadratic shift as well as the  $t_s$  dependence on spin, this becomes the traditional Harper-Hofstadter Hamiltonian

$$H = - \sum_{j,m} t_x e^{i\phi_{AB}m} |j+1, m\rangle \langle j, m| + t_s |j, m+1\rangle \langle j, m| + h.c. \quad (6.8)$$

We can transform this Hamiltonian into momentum space along  $\mathbf{e}_x$  by plugging the Fourier transform formula

$$|j, m\rangle = \frac{1}{\sqrt{N}} \sum_{k_j} e^{-ik_j j} |k_j, m\rangle \quad (6.9)$$

into the above Hamiltonian to obtain

$$H = -\frac{1}{N} \sum_{k_j, m} t_m |k_j, m+1\rangle \langle k_j, m| + h.c. + 2t_x \cos(k_j - \phi_{AB}) |k_j, m\rangle \langle k_j, m| + A_m |k_j, m\rangle \langle k_j, m| \quad (6.10)$$

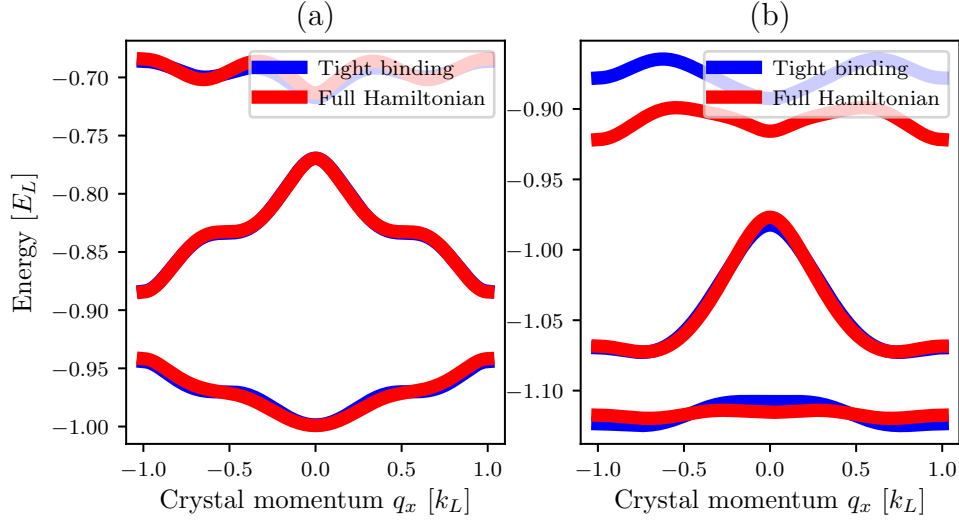


Figure 4: Band structure of the tight binding versus full Hamiltonian.  $V_0 = 6.0E_L$ , giving  $t_x = 0.1E_L$ ,  $\hbar\delta = 0$ ,  $\hbar\epsilon = 0.02E_L$ ,  $\hbar\Omega = 0.5E_L$ . (a)  $F = 1$ , fitted value  $t_s = 0.154E_L$ . (b)  $F = 2$ , fitted value  $t_s = 0.284$ .

To go from the full Hamiltonian, eqn. 6.4, to the tight binding Hamiltonian we must find appropriate values for  $t_s$  and  $t_x$ . We find  $|t_x|$  by treating the 1-D lattice independently, and matching the tight binding band to the lowest full lattice band. For most of the experiments described in the chapter, the lattice depth was  $V_0 = 6E_L$ , corresponding to  $|t_x| \approx 0.01E_L$ . To find the appropriate value of  $t_s$ , we fit the full synthetic dimensions band structure to the tight binding band structure eqn. 6.10 with  $t_s$  as a free parameter.

Figure 4 shows the overlaid band structure of the full Hamiltonian, eqn. 6.4, and the best fit tight binding band structure, eqn. 6.10. To fit, we minimize the square difference between the energies in the lowest two bands, relevant to our experiment.

### 6.3 Eigenstates of the synthetic 2-D lattice

After calibrating the synthetic dimensional lattice via pulsing, we can study the eigenstates of the lowest band of the system by adiabatically loading, i.e. ramping both the lattice and Raman or rf coupling on on a time scale slow compared to the magnetic band spacing. Along the synthetic direction, in the  $F = 1$  manifold, there are no  $m = \pm 2$  sites. This can be thought of as hard wall boundary conditions at the  $m = \pm 2$  sites, confining the atoms in the allowed  $m = 0, \pm 1$  sites. Therefore, we can consider the position eigenstates along the synthetic direction in relation to eigenstates of a square well potential.

Figure 5a shows a time-of-flight image of an adiabatically loaded synthetic dimensions lattice eigenstate with rf coupling along the synthetic direction. The vertical axis is single site resolved spin states  $m$ . The horizontal axis is momentum along the  $\mathbf{e}_x$  direction. Note that for each site  $m$  the distribution of momenta  $k_x$  is symmetric. Figure 5b shows the fractional population in each site  $m$ , summed over all momenta  $k_x$ . In the case of rf coupling,  $\phi_{AB} = 0$  and the effective magnetic flux  $\Phi_{AB}/\Phi_0 = 0$ . Therefore, the fractional population along the spin direction looks simply like a discretized ground state probability distribution of the square well potential.

Figure 5c-h shows analogous data with Raman coupling along the synthetic direction. Figure 5d,g are the time-of-flight image and corresponding fractional populations of atoms adiabatically loaded from the  $m_F = 0$  spin state, corresponding to the central minimum ( $q = 0$ ) of the lowest band in Figure 2b. There are two key differences between this case and the rf case Figure 5a-b. First, the momenta of the different spin states are no longer symmetric, as explained in sec. 6.2.3. Second, the fractional populations in Figure 5g are no longer simply the discretized ground state probability distribution of the square well potential—it is a narrowed version

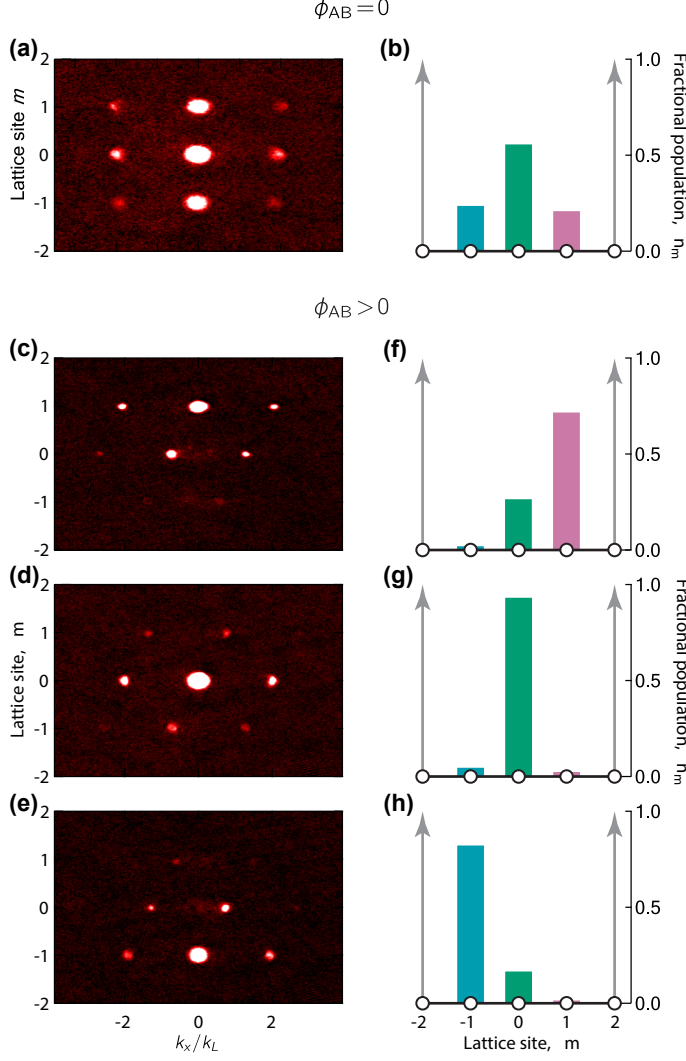


Figure 5: Eigenstates of the synthetic dimensions lattice. Left column: time-of-flight images, with position along  $\mathbf{e}_s$  on the vertical axis and momentum along  $\mathbf{e}_s$  on the horizontal. Right column: fractional populations in each site  $m$ . (a,b) Rf coupling, resulting in  $\phi_{AB} = 0$ . (c,f) Raman coupling, resulting in  $\phi_{AB} > 0$ , adiabatically loaded from the  $m_F = 1$  state. (d,g) Raman coupling, resulting in  $\phi_{AB} > 0$ , adiabatically loaded from the  $m_F = 0$  state. (e,h) Raman coupling, resulting in  $\phi_{AB} > 0$ , adiabatically loaded from the  $m_F = -1$  state.



of it, more strongly concentrated in the  $m = 0$  site.

This can be understood by analogy with a 2D electron system in a perpendicular magnetic field, confined in one dimension with hard walls. Along the confined direction, the wavefunction is localized to the scale of the magnetic length  $l_B = \sqrt{\hbar/qB}$ , with the center position at  $k_x l_B^2$  in the bulk state, where  $\hbar k_x$  is the electrons canonical momentum. In our system, the magnetic length  $l_B = \sqrt{a^2 \Phi_0 / 2\pi \Phi_{AB}}$ , or in units of the lattice period  $a$ ,  $l_B^* = \sqrt{3/2\pi}$ ; this explains the narrowing of the bulk state in Figure 5g.

In the 2D electron system, at large  $|k_x|$ , the electron becomes localized near the edges, lifting the degeneracy of the otherwise macroscopically degenerate Landau levels. In our case, stable edge states appeared as the additional minima in Figure 2b, at  $q \approx \pm 0.66 k_L$ . We loaded these edge states by starting in the  $m_F = \pm 1$  states before adiabatically turning on the synthetic dimensions lattice to obtain eigenstates displayed in Figure 5c,f and Figure 5e,h respectively. These edge states predominantly occupy the edge sites in the synthetic direction, and are strongly confined there due to the narrow magnetic length. These localized edge states are the analog to the current-carrying edge states in fermionic integer quantum Hall effect systems [24].

## 6.4 Chiral edge currents

The same pulsing procedure that was used for calibration (sec. 6.2.3) can also be interpreted by analogy with the 2-D electron system. Figure 6a shows schematically what happens atoms are loaded from the  $m = 0$  site into the lattice and tunneling along the synthetic dimension is pulsed on. Atoms begin analogues of cyclotron orbits, tunneling out into the edge  $m = \pm 1$  sites and tunneling back to the bulk  $m = 0$  state. The fractional populations in the three  $m$  sites as a function of time are shown in Figure 6b.

We performed this experiment for three different magnetic flux values: with rf coupling giving  $\Phi_{AB}/\Phi_0 = 0$ , with Raman coupling giving  $\Phi_{AB}/\Phi_0 \approx 4/3$  and with inverted Raman coupling giving  $\Phi_{AB}/\Phi_0 \approx -4/3$ . The inverted Raman coupling was accomplished by switching the roles of the two Raman beams (see Figure ??a): the right going beam frequency was changed to  $2\pi(\omega + \Delta\omega)$  and the left going beam frequency to  $2\pi\omega$ , resulting in the opposite recoil momentum for the same spin flip, flipping the direction of the effective magnetic field.

We define the current  $I_{m=\pm 1} = n_m \langle v_m \rangle$ , where  $n_m$  is the fractional population in site  $m$  and  $\langle v_m \rangle$  is the expectation value of velocity along  $\mathbf{e}_x$  for atoms in sites  $m$ , as depicted in Figure 6a. The velocity is derived from the momentum measured in time-of-flight images. The chiral current of the system is then defined as  $\mathcal{I} = I_1 - I_{-1}$ . We calculate this chiral current for data in Figure 6b, with  $\Phi_{AB}/\Phi_0 \approx 4/3$ , displayed in red dots in Figure 6c. Atoms in the edge sites  $m = \pm 1$  exhibit chiral motion, therefore the resulting chiral current is directly proportional to the fractional population in those sites and oscillates as a function of time in concert with the oscillation in Figure 6b. in Figure 6c also includes data for the  $\Phi_{AB}/\Phi_0 \approx -4/3$  (solid black dots indicate data and solid black lines are from theory) and  $\Phi_{AB}/\Phi_0 = 0$  (empty black dots). As seen in the figure, reversing the direction of the effective magnetic flux reverses the direction of the chiral current, and turning off the magnetic flux results in no net chiral current. The chiral current  $\mathcal{I}$  is normalized here by the tunneling velocity  $2t_x/\hbar k_L$ .

As the chiral current  $\mathcal{I}$  is proportional to the edge state population, we plot it as a function of the expectation value of the absolute value of  $m$ ,  $\langle |m| \rangle$ , in Figure 6d. As expected, the chiral current is linear and positive for  $\Phi_{AB}/\Phi_0 \approx 4/3$ , negative for  $\Phi_{AB}/\Phi_0 \approx -4/3$ , and zero for  $\Phi_{AB}/\Phi_0 = 0$ . We call this slope  $\mathcal{S}$ . We then study the dependence of the chiral current on the strength of tunneling along the synthetic dimension, in units of the real axis tunneling  $t_s/t_x$ . We refer to this as

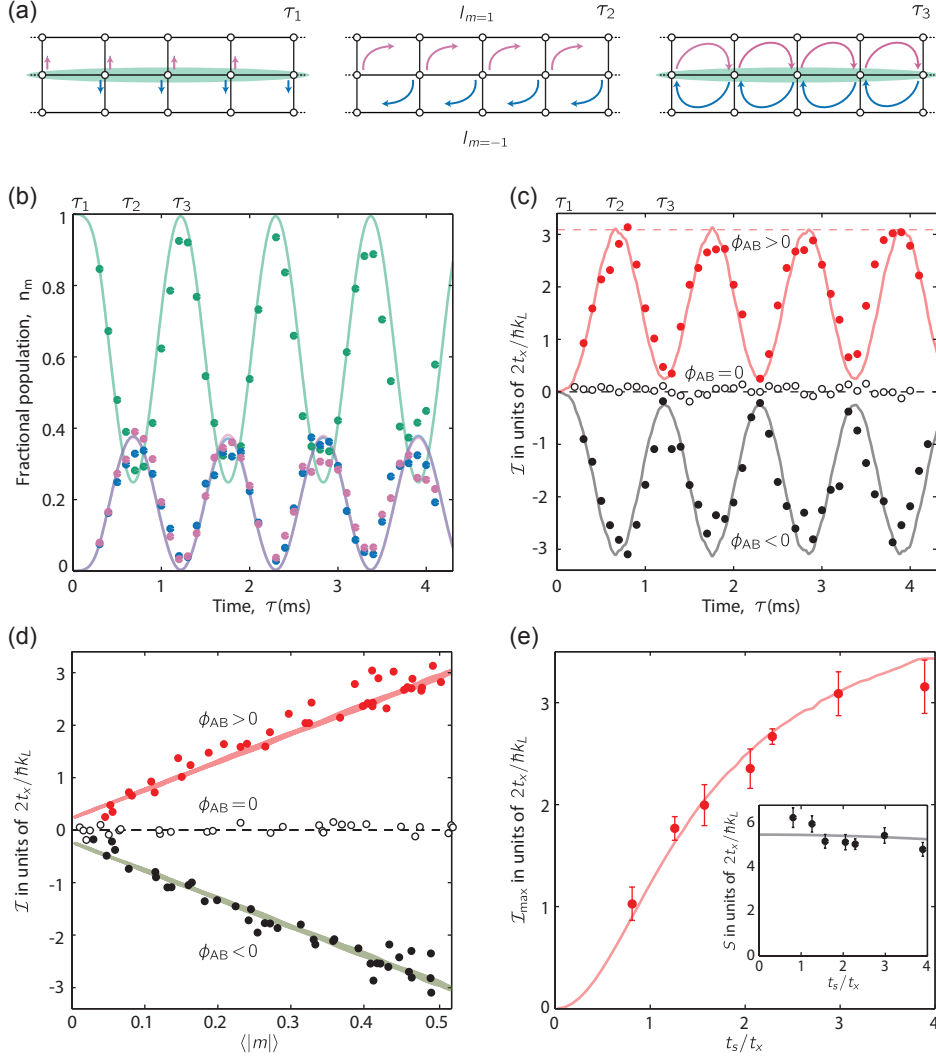


Figure 6: Measuring chiral currents in synthetic dimensions. (a) Schematic of the formation of chiral currents when the system is loaded into the bulk  $m = 0$  site and tunneling along  $\mathbf{e}_s$  is turned on suddenly. (b) Fractional population in each spin state as a function of time for a system with  $\phi_{AB} > 0$ . Dots represent data and lines represent theory, with parameters  $\hbar\Omega = 0.5E_L$ ,  $V_0 = 6E_L$ ,  $\hbar\delta = 0.001E_L$ , and  $\hbar\epsilon = 0.05E_L$ . (c) Chiral current  $\mathcal{I}$  as a function of time for  $\phi_{AB} > 0$  (red)  $\phi_{AB} = 0$  (empty black dots) and  $\phi_{AB} < 0$  (solid black). (d) Chiral current  $\mathcal{I}$  as a function of  $\langle |m| \rangle$  for the three values of  $\phi_{AB}$ . Solid lines calculated from theory, with the same parameters as in (b) for  $\phi_{AB} \neq 0$ , and with parameters  $\hbar\Omega = 0.33E_L$ ,  $V_0 = 6E_L$ ,  $\hbar\delta = -0.01E_L$ , and  $\hbar\epsilon = 0.05E_L$  for  $\phi_{AB} = 0$ . (e) Peak chiral current  $\mathcal{I}_{\max}$  as a function of tunneling asymmetry  $t_s/t_x$ . Inset: slope of best fit lines of current  $\mathcal{I}$  as a function of  $\langle |m| \rangle$  (as in (d)) as a function of tunneling asymmetry  $t_s/t_x$ : nearly independent.

the tunneling anisotropy: the asymmetry between the two dimensions. As shown in the inset to Figure 6e, the slope  $\mathcal{S}$  of the chiral current as a function of  $\langle|m|\rangle$  is practically independent of the tunneling anisotropy. The small deviation from a flat line is explained by the deviation of our system from the tight binding model. However, the maximal chiral current attained during the pulsing experiment,  $\mathcal{I}_{\text{max}}$ , depends strongly on the tunneling anisotropy (see Figure 6e). This is because the maximum fractional population in the edge states  $\langle|m|\rangle$  increases with increased  $t_s$ . The increase is approximately linear at first, and then saturates at large  $t_s/t_x$  when the fractional population in the edge states  $m = \pm 1$  approaches 1.

## 6.5 Observation of skipping orbits

Semiclassically, electrons in a 2-D material pierced by a magnetic field can be described in terms of cyclotron orbits in the bulk, as described in the previous section, and skipping orbits on the edge. Skipping orbits arise from electrons on the edge beginning cyclotron orbits, but hitting the edge of the system and being reflected and beginning the next cyclotron orbit. Due to the chirality of the cyclotron orbits, this results in the skipping orbits travelling in one direction along the top edge and in the opposite direction along the bottom edge.

We observed an analogue of these skipping orbits in our system. We performed the same experiment, pulsing on tunneling along the synthetic dimension, but this time initializing the system on the edge, as shown schematically in Figure 7a. To populate these states, we initially applied a detuning  $\hbar\delta = \pm 0.087E_L$ , tilting the potential along the synthetic direction as shown in Figure 7b. This made the initial state,  $m = -1$  in the figure, a potential minimum. We then pulsed on the tunneling and observed the resulting dynamics.

Figure 7c shows the expectation value of position along  $\mathbf{e}_s$  as a function of time during the pulsing experiment. This expectation value is obtained by calculating

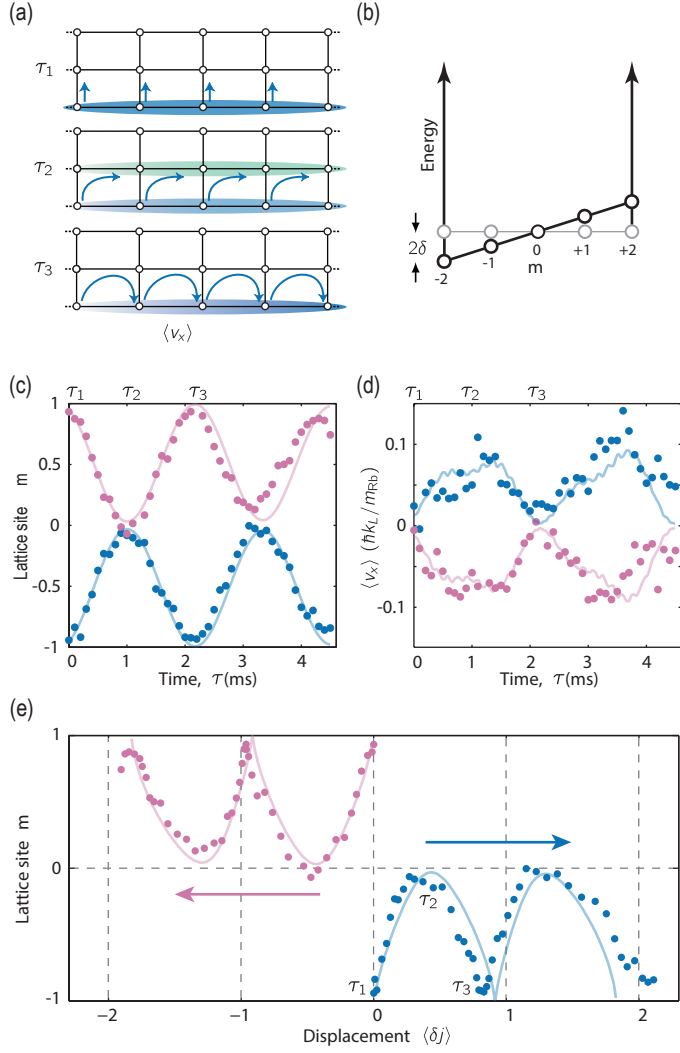


Figure 7: Imaging skipping orbits. (a) Schematic of pulsing experiment when atoms are initialized on the edge. (b) Schematic of the tilted box potential applied along the synthetic direction. (c) Expectation value of position along  $\mathbf{e}_s$ ,  $\langle m \rangle$ , as a function of pulse time for atoms initialized in the  $m = +1$  (red) and  $m = -1$  (blue) states. Dots represent data and lines are from theory with parameters  $\hbar\Omega = 0.41E_L$ ,  $V_0 = 5.2E_L$ ,  $\hbar\delta = \pm 0.087E_L$ , and  $\hbar\epsilon = 0.13E_L$ . (d) Expectation value of the group velocity along  $\mathbf{e}_x$ ,  $\langle v_x \rangle$ , for the same data as in (c). (e) Expectation value of displacement along  $\mathbf{e}_x$ ,  $\langle \delta j \rangle$  in units of lattice spacing, for the same data as in (c) and (d). The displacement was obtained by integrating  $\langle v_x/a \rangle$ , where  $a$  is the period of the optical lattice. Atoms initialized in  $m = -1$  performed skipping orbits to the left, while atoms starting in  $m = +1$  travelled to the right.

the fractional population  $n_m$  on each site  $m$  and summing  $\langle m \rangle = \sum_m m n_m$ . The red dots were obtained from an experiment where the atoms were initialized in the  $m = 1$  site. The blue dots were obtained by starting in the  $m = -1$  site. The expected position oscillated with time, as expected for Rabi oscillations. The same data was then used to extract the expected group velocity along  $\mathbf{e}_x$ ,  $\langle v \rangle = \sum_m n_m \langle v_m \rangle$  as a function of time. This is shown in Figure 7d. The group velocity oscillated with the expected position  $\langle m \rangle$ , and was positive for experiments starting in  $m = -1$  and negative for experiments starting in  $m = 1$ .

We obtain the expected displacement in units of the lattice spacing  $a$ ,  $\langle \delta j \rangle$  along  $\mathbf{e}_x$  as a function of time by directly integrating the expected group velocity. The resulting displacement is shown in Figure 7e. As seen in the figure, for experiments initialized in  $m = 1$ , the atoms began cyclotron orbits, but reflected off the edge and performed skipping orbits towards the left. Likewise, atoms initialized in  $m = -1$  performed skipping orbits along the opposite edge and in the opposite direction. This experiment presents the first direct observation of skipping orbit motion.

## Bibliography

- [1] Daniel Adam Steck. Rubidium 87 d line data. Available online, <http://steck.us/alkalidata>, April 2018. revision 2.1.5.
- [2] K. Jiménez-García, L. J. LeBlanc, R. A. Williams, M. C. Beeler, A. R. Perry, and I. B. Spielman. Peierls substitution in an engineered lattice potential. *Phys. Rev. Lett.*, 108:225303, May 2012.
- [3] H.J. Metcalf and P. van der Straten. *Laser Cooling and Trapping*. Graduate Texts in Contemporary Physics. Springer New York, 1999.
- [4] N.W. Ashcroft and N.D. Mermin. *Solid State Physics*. Saunders College, Philadelphia, 1976.
- [5] Nicola Marzari, Arash A. Mostofi, Jonathan R. Yates, Ivo Souza, and David Vanderbilt. Maximally localized wannier functions: Theory and applications. *Rev. Mod. Phys.*, 84:1419–1475, Oct 2012.
- [6] Karina Jimenez-Garcia. *Artificial Gauge Fields for Ultracold Neutral Atoms*. PhD thesis, Joint Quantum Institute, National Institute of Standards and Technology, and the University of Maryland, 2012.

- [7] Daniel Adam Steck. Quantum and atom optics. Available online at <http://steck.us/teaching>, January 2015. revision 0.12.2.
- [8] K. v. Klitzing, G. Dorda, and M. Pepper. New method for high-accuracy determination of the fine-structure constant based on quantized hall resistance. *Phys. Rev. Lett.*, 45:494–497, Aug 1980.
- [9] D. J. Thouless, M. Kohmoto, M. P. Nightingale, and M. den Nijs. Quantized hall conductance in a two-dimensional periodic potential. *Phys. Rev. Lett.*, 49:405–408, Aug 1982.
- [10] Douglas R. Hofstadter. Energy levels and wave functions of bloch electrons in rational and irrational magnetic fields. *Phys. Rev. B*, 14:2239–2249, Sep 1976.
- [11] M. C. Geisler, J. H. Smet, V. Umansky, K. von Klitzing, B. Naundorf, R. Ketzmerick, and H. Schweizer. Detection of a landau band-coupling-induced rearrangement of the hofstadter butterfly. *Phys. Rev. Lett.*, 92:256801, Jun 2004.
- [12] B. Hunt, J. D. Sanchez-Yamagishi, A. F. Young, M. Yankowitz, B. J. LeRoy, K. Watanabe, T. Taniguchi, P. Moon, M. Koshino, P. Jarillo-Herrero, and R. C. Ashoori. Massive Dirac Fermions and Hofstadter Butterfly in a van der Waals Heterostructure. *Science*, 340:1427, 2013.
- [13] P. Zoller D. Jaksch. Creation of effective magnetic fields in optical lattices: the hofstadter butterfly for cold neutral atoms. *New Journal of Physics*, 5(1):56, 2003.
- [14] M. Aidelsburger, M. Atala, M. Lohse, J. T. Barreiro, B. Paredes, and I. Bloch. Realization of the hofstadter hamiltonian with ultracold atoms in optical lattices. *Phys. Rev. Lett.*, 111(18):185301–, October 2013.



- [15] Hirokazu Miyake, Georgios A. Siviloglou, Colin J. Kennedy, William Cody Burton, and Wolfgang Ketterle. Realizing the harper hamiltonian with laser-assisted tunneling in optical lattices. *Phys. Rev. Lett.*, 111:185302, Oct 2013.
- [16] Gregor Jotzu, Michael Messer, Remi Desbuquois, Martin Lebrat, Thomas Uehlinger, Daniel Greif, and Tilman Esslinger. Experimental realization of the topological haldane model with ultracold fermions. *Nature*, 515(7526):237–240, Nov 2014.
- [17] M Aidelsburger, M Lohse, C Schweizer, M Atala, J T Barreiro, S Nascimbène, N. R. Cooper, I. Bloch, and N. Goldman. Measuring the Chern number of Hofstadter bands with ultracold bosonic atoms. *Nature Physics*, 11(2):162–166, December 2014.
- [18] M. Mancini, G. Pagano, G. Cappellini, L. Livi, M. Rider, J. Catani, C. Sias, P. Zoller, M. Inguscio, M. Dalmonte, and L. Fallani. Observation of chiral edge states with neutral fermions in synthetic hall ribbons. *Science*, 349(6255):1510–, Sep 2015.
- [19] M Hafezi, S Mittal, J Fan, A Migdall, and J M Taylor. Imaging topological edge states in silicon photonics. *Nat. Photon.*, 7(12):1001–1005, October 2013.
- [20] A. Celi, P. Massignan, J. Ruseckas, N. Goldman, I.B. Spielman, G. Juzeliunas, and M. Lewenstein. Synthetic gauge fields in synthetic dimensions. *Phys. Rev. Lett.*, 112(4):043001–, Jan 2014.
- [21] B. K. Stuhl, H.-I. Lu, L. M. Ayccock, D. Genkina, and I. B. Spielman. Visualizing edge states with an atomic bose gas in the quantum hall regime. *Science*, 349(6255):1514–, Sep 2015.
- [22] Y. Aharonov and D. Bohm. Significance of electromagnetic potentials in quantum theory. *Phys. Rev.*, 115:485, 1959.

- [23] Yakir Aharonov and Ady Stern. Origin of the geometric forces accompanying berry's geometric potentials. *Phys. Rev. Lett.*, 69(25):3593–3597, 1992.
- [24] Dario Hgel and Beln Paredes. Chiral ladders and the edges of quantum Hall insulators. *Phys. Rev. A*, 89(2):023619, 2014.